Construction and Building Materials 392 (2023) 130880

Contents lists available at ScienceDirect

Construction and Building Materials

journal homepage: www.elsevier.com/locate/conbuildmat

Experimental characterisation of dry-joint masonry structures: Interface stiffness and interface damping

Georgios Vlachakis [a], Carla Colombo [a], Anastasios I. Giouvanidis [a,*], Nathanaël Savalle [a,b], Paulo B. Lourenço [a]

[a] University of Minho, ISISE, ARISE, Department of Civil Engineering, Guimarães, Portugal
[b] Université Clermont Auvergne, Clermont Auvergne INP, CNRS, Institut Pascal, F-63000 Clermont-Ferrand, France

ARTICLE INFO

Keywords:
Normal interface stiffness
Tangential interface stiffness
Interface damping
Masonry structures
Dry-joint
Contact mechanics
Non-linear dynamics
Joint closure tests
Shear-box tests
Vibration-based tests

ABSTRACT

The accurate description of the dynamics of dry-joint masonry structures strongly relies on the characterisation of the interaction at the units' interfaces. Several experimental techniques are available for estimating the mechanical properties of the interface (i.e. stiffness and damping), yet, their reliability remains questionable given the lack of comprehensive comparative studies. This work presents an extensive experimental campaign on the meso-scale mechanics of dry-joint interfaces and quantifies both the interface stiffness and interface damping. Importantly, this paper reveals, for the first time, remarkable agreement of the interface stiffness estimated by inherently different experimental methods, namely deformation-based and vibration-based. Thus, it paves the way for the formulation of reliable constitutive laws that govern structural response in numerical modelling of dry-joint masonry structures.

1. Introduction

Masonry is one of the oldest construction materials. The wide variety of components together with the relatively simple construction process make it extensively widespread all over the world. Among the construction methods, the use of unreinforced dry-joint masonry has been commonly adopted, either in real-life structures [1] or in experimental programmes aiming at characterising regular low-tension masonry structures [2–5]. In this case, the units interact with each other without any mortar, making the dry-joint solely responsible for the load transmission. A reliable description of the response of dry-joint masonry structures faces marked challenges [6–8]. Specifically, one should define both the units' behaviour and the interaction among them. The former, although usually non-trivial, is assumed to be common practice [9]. On the contrary, the description of the mechanical interaction among different units lacks established methods and, importantly, plays an essential role in the global response of such assemblies [10]. Thus, the definition of reliable constitutive laws that define the units' interaction could greatly facilitate the description of the non-linear behaviour of such structures.

Contact mechanics spans over different scales, i.e. micro, meso, and macro [11], which results in the adoption of various types of interaction models ([12–19] and references therein). Specifically, the micro-scale framework presumes the definition of the topography of the granular asperities (in the order of 10^{-6} m), together with the properties of the bulk material, in order to derive the interface behaviour [11,15,16]. Yet, such an approach lies far from the engineering interest of masonry structures, where the interacting units commonly stand between 10^{-2} and 10^{0} m. Alternatively, the focus of the present work on the dynamics of masonry structures resorts to meso-scale formulations. This framework presumes the definition of the i) frictional properties, ii) interface stiffness, and iii) interface energy losses, while the influence of the granular asperities at the micro-scale is of interest only in a phenomenological sense. Frictional properties, such as friction angle and dilatancy, have traditionally attracted the greatest attention [7,8,18,20–23] since they considerably influence the failure of masonry structures under static loads. However, a more holistic description of the structural dynamic response strongly relies also upon the interface stiffness and interface energy losses [10,24–29]. Altogether, they compose the essential parameters of any contact model that follows an explicit

* Corresponding author.
E-mail addresses: giorgovlachaki@gmail.com (G. Vlachakis), carla.colombo95@gmail.com (C. Colombo), agiouvanidis@civil.uminho.pt (A.I. Giouvanidis), nathanael.savalle@uca.fr (N. Savalle), pbl@civil.uminho.pt (P.B. Lourenço).

https://doi.org/10.1016/j.conbuildmat.2023.130880
Received 11 August 2022; Received in revised form 21 January 2023; Accepted 25 February 2023
Available online 25 May 2023

description of the contact process via a meso-scale formulation [14] (e.g. the Discrete Element Modelling [30]). Nevertheless, despite the stress-dependent nature of the interface stiffness [16,31–33], researchers tend to adopt constant values on an empirical basis [34,35] or after a posteriori fitting to a reference response of much higher complexity [26,27,36], rather than resorting to experimental characterisation campaigns. Similarly, besides interface energy losses arising from friction, which are adequately described by the frictional properties, damping models of dry-joint interfaces are rarely defined on an experimental basis, but are rather calibrated [25,29], fitted [27,36], or even omitted [26,37,38]. Hence, it becomes clear that experimental studies on the interface stiffness and interface damping are of paramount importance to reliably describe the complex non-linear dynamic behaviour of dry-joint masonry structures.

Different engineering fields have shown interest to experimentally characterise dry-joint interface properties, resulting in various approaches, which can be categorised as: i) deformation-based [21,39–43], ii) vibration-based [26,44–46], and iii) wave-based [31,47–52]. The deformation-based approach directly measures the interface deformation triggered by the application of a prescribed load or displacement. This straightforward approach has been widely adopted in literature and gives a direct correlation between the interface deformation and the normal/tangential stress, and hence the normal/tangential interface stiffness and the interface hysteretic energy losses. The vibration-based (or contact resonance) approach allows the indirect estimation of both interface stiffness and interface damping. Specifically, it measures the vibrations of a system using dynamic identification techniques and consequently estimates the interface properties by describing its dynamics (i.e. frequencies of vibration, mode shapes, and damping). Finally, the wave-based approach is a non-invasive method based on the emission of waves through the joint between two bodies. This approach assumes that the normal/tangential interface stiffness is proportional to the longitudinal/transversal reflection coefficient, the frequency of emission, the wave speed, and the material density.

Despite the existence of different experimental approaches that quantify the interface properties of contacting bodies, the studies that have compared their outcomes are scarce [44,50,52]. In particular, Mulvihill et al. [52] noticed that the tangential and normal interface stiffness estimated through the ultrasound wave-based approach are about 2.7 and 3.5 times, respectively, higher than the pertinent stiffness derived from deformation-based measurements. Fantetti et al. [50] also observed a similar mismatch between (ultrasound) wave-based and deformation-based techniques, with the former providing tenfold higher tangential stiffness estimations compared to the latter. These authors attributed such a large discrepancy to factors such as the influence of the bulk deformation in the hysteresis loops and/or compliance effects provided by the test rigs, among others. Recently, Gimpl et al. [44] compared vibration-based methods against deformation-based measurements of stiffness, yet, agreement was not achieved owing to the experimental setup. In particular, local interface resonances at low vibration amplitudes led to inaccurate relative displacement measurements and thus misleading stiffness estimations. Therefore, it becomes apparent that there are significant discrepancies among different methods in the experimental estimation of the interface properties, which essentially govern the non-linear dynamic behaviour of contacting bodies.

This study presents an extensive experimental campaign on limestone specimens with dry-joint interfaces. Both interface stiffness and interface damping are quantified and discussed, providing an insight into their complex behaviour. The investigation expands over a wide range of normal stress levels, while other physical conditions, e.g. surface roughness, wear phenomena and moisture conditions, remain constant [31,33,45,53]. Importantly, this work compares inherently different experimental methods aiming to provide a critical appraisal of the methodologies used to estimate the interface properties. It thus provides a general experimental framework with detailed guidelines for the characterisation of dry-joint interfaces of any masonry-like material. Finally, it is envisaged that the outcomes of the methodology can facilitate the formulation of experimentally informed constitutive laws for numerical modelling.

This paper is organised as follows: Section 2 introduces the experimental campaign, including the theoretical basis of the experimental methodologies, setup description, and testing protocols. Section 3 provides the results and findings related to the interface stiffness, while Section 4 focuses on the interface damping outcomes. Finally, Section 5 summarises the main conclusions of this work together with a brief discussion highlighting merits and shortcomings of the employed methods and potential future research directions.

2. Experimental campaign

2.1. Material characterisation

This work adopts specimens made of hard limestone [54]. Such material is representative of a variety of heritage masonry structures around the world ([55–57] among others). At a meso-scale, the specimens' surfaces appear heterogeneous and characterised by distributed shell segments and fossil debris (Fig. 1a). The material density is $\rho = 2238$ kg/m^3. The material compressive strength f_c is evaluated through uniaxial compressive tests [58] on five limestone cylinders, cored from a parallelepiped specimen. After the coring process, the moisture condition is homogenised thanks to a temperature-controlled oven drying process. The cylinders are 173.5 mm (Coefficient of Variation CoV = 1.1 %, Number of samples N = 5) in height, and 69.6 mm (CoV = 0.0 %, N = 5) in diameter, leading to a height/diameter ratio between 2.0 and 2.5 [58]. Finally, an average compressive strength f_c equal to 47.6 MPa is found (CoV = 7.9 %, N = 5).

Five uniaxial compression tests on the cylindrical specimens are conducted to obtain the elastic modulus E_{stone} [58]. Each limestone cylinder is subjected to three force-controlled loading–unloading cycles

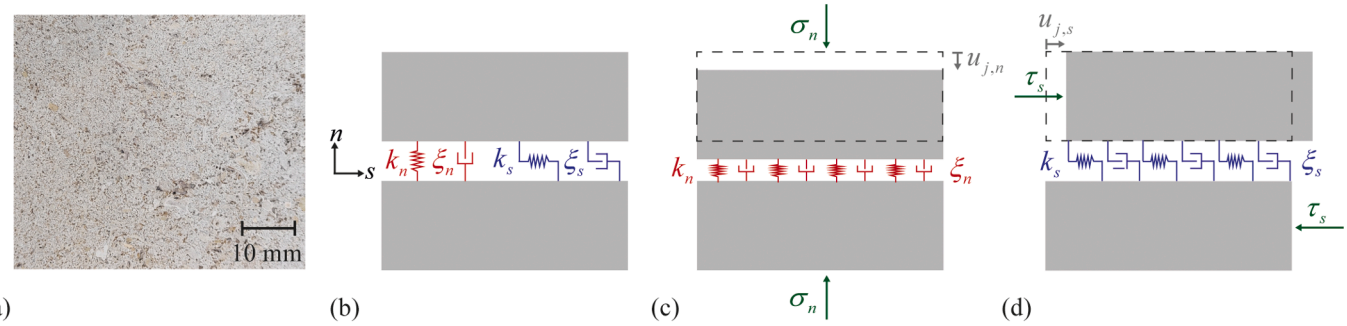

Fig. 1. (a) Representative limestone surface, (b) adopted meso-scale mechanical scheme that describes the dry-joint interaction mechanism, (c) normal behaviour of interface under normal stress, and (d) tangential behaviour of interface under shear and constant normal stress.

up to 1/3 of the compressive strength f_c, while three Linear Variable Differential Transformers (LVDTs) record the displacement. An averaged value of 32.7 GPa is measured (CoV = 4.7 %, N = 5).

2.2. Interface mechanical scheme

The present work assumes a meso-scale mechanical scheme to describe the dry-joint interaction of masonry specimens. Fig. 1b illustrates the examined interaction mechanism of two bodies in contact, idealised with a uniformly distributed spring-like scheme over the contact interface. The interaction is characterised by two interface stiffness parameters k_n and k_s (expressed in N/m^3, or equivalently Pa/m), acting in the normal and tangential directions, respectively. Furthermore, dissipative phenomena taking place at the interface are described through a viscous-type representation, herein denoted with the unitless damping ratios ξ_n and ξ_s for the normal and tangential directions, respectively (Fig. 1b). More specifically, the energy losses are presumed to be proportional to the relative velocity of the interacting bodies, and therefore reproduce a dashpot-like definition. It is worth underlining that this dashpot-like scheme is a convenient way to simulate dissipative phenomena at the meso-scale, since it allows a phenomenological description of energy losses both of dynamic/vibration and hysteretic nature [59]. The aforementioned parameters are in force only during contact, while they are nullified upon separation. Finally, although the micro-scale characteristics, such as the granular asperities of the surfaces in contact [11], are not explicitly studied herein, their effects are inherently considered from a meso-scale phenomenological perspective.

2.3. Deformation-based approach

Deformation-based experimental testing methods are probably the most common way to characterise the interface stiffness of dry-joints [21,39–44,50]. Such methods measure the dry-joint response by imposing a relative displacement at the interface through the application of load. Normal and tangential responses of dry-joint require different tests (Fig. 1b-d). Specifically, in the normal direction (Fig. 1c), the two bodies are compressed with a normal stress σ_n causing a joint closure $u_{j,n}$. On the other hand, in the tangential direction (Fig. 1d), the two bodies are sheared with a stress τ_s resulting in a joint relative displacement $u_{j,s}$ while maintaining a constant normal stress σ_n. Hence, the interface stiffness k_n and k_s are defined as:

$$k_n = \frac{d\sigma_n}{du_{j,n}},\ k_s = \frac{d\tau_s}{du_{j,s}} \tag{1}$$

Deformation-based tests additionally allow the measurement of hysteretic energy losses that occur at the interface, which can be quantified through the hysteresis loops of the load-deformation response. Modelling such hysteretic losses can be explicitly achieved using constitutive laws that describe the experimental load-deformation response in detail. However, constitutive laws often adopt a simplified representation of the actual behaviour, and thus an implicit consideration of the omitted hysteretic energy losses should accompany such models [59]. The most common approach is the use of an equivalent viscous damping model [60], in line with the dashpot-like scheme adopted herein (Fig. 1b). Specifically, the hysteretic viscous damping ratio that satisfies energy equivalence reads $\xi_{hyst} = \frac{1}{4\pi}\frac{E_d}{E_e}$, where E_d corresponds to the energy dissipated during a complete cycle of the hysteretic system and E_e is the elastic stored energy at maximum response. Nevertheless, since detachment of the dry-joint occurs with no tensile stress, for the unilateral definition of the viscous dashpot $\xi_{hyst,uni}$ (i.e. herein the presumed scheme in the normal direction), the dissipated energy E_d is multiplied by 2 in order to dissipate the aimed energy solely during the loading–unloading cycle:

$$\xi_{hyst,uni} = \frac{1}{2\pi}\frac{E_d}{E_e} \tag{2}$$

Conceptually, this energy equivalence between hysteretic and viscous damping losses builds on the assumption that the damped system experiences stable periodic oscillations at resonance, and thus undergo steady-state response [60,61]. As a matter of fact, the method is a simplification of the hysteretic dissipation [62], while for a more accurate representation of the energy losses, one should preferably provide a refined hysteretic constitutive law.

2.3.1. Joint closure tests

The interface properties in the normal direction of contact (i.e. k_n and $\xi_{hyst,n}$) are evaluated using joint closure compression tests (Fig. 2). More specifically, the well-known setup used for the determination of the elastic modulus [58] is modified by introducing two specimens in contact with a dry-joint (Fig. 2). Seven cylindrical specimens are used (Fig. 2a), with a diameter of 64.7 mm (CoV = 1.2 %, N = 7) and height 80.5 mm (CoV = 1.8 %, N = 7). An actuator mounted with a load cell and three LVDTs arranged at an angle of 120° in plan are employed to measure the applied force and relative displacement, respectively

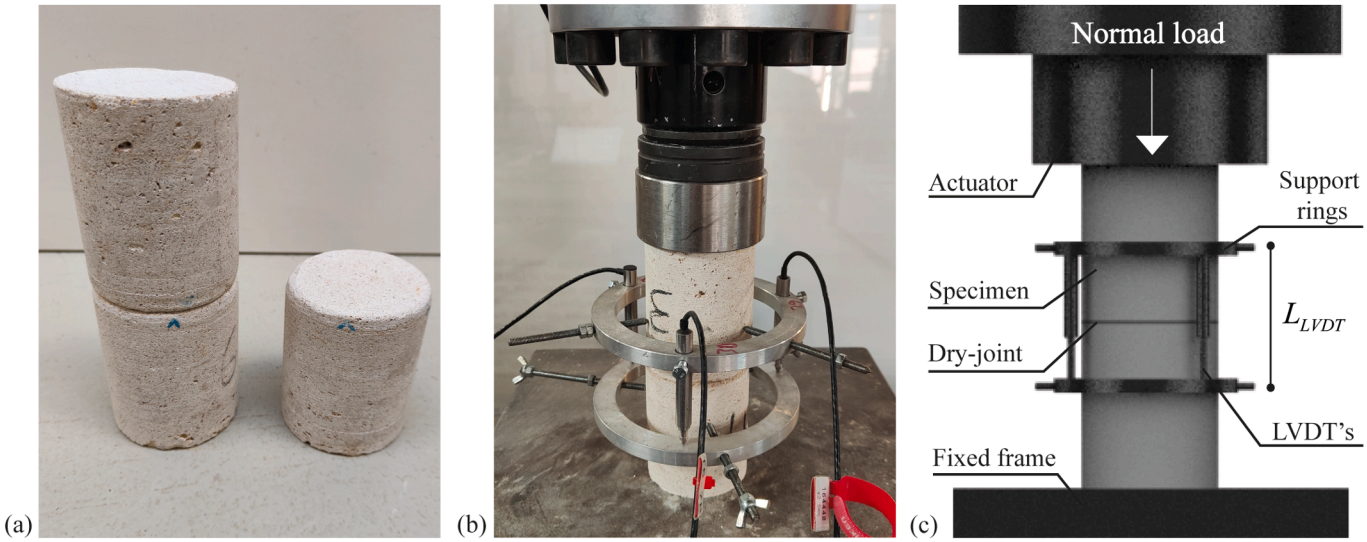

Fig. 2. Joint closure tests: (a) adopted cylindrical specimens, (b) experimental setup, and (c) schematic representation of the main components.

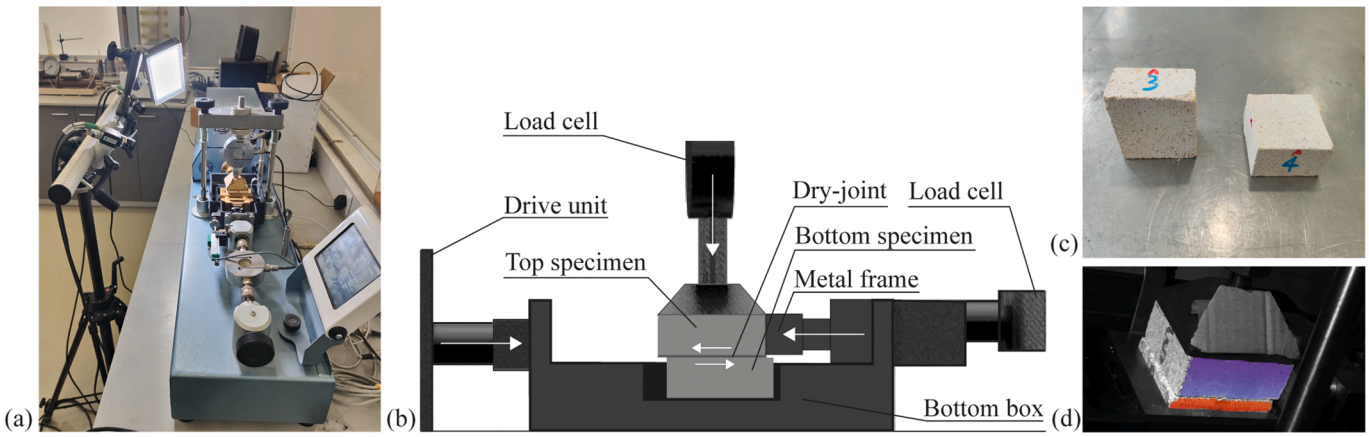

Fig. 3. Shear-box tests: (a) experimental shear-box (27-WF21E80 SHEARMATIC) test setup, (b) schematic representation of the main components, (c) adopted specimens, and (d) representative example of the DIC acquisition.

(Fig. 2b-c). This setup implies that the bulk deformability of the two bodies in contact is also introduced in the acquired measurement u_{LVDT} (from the LVDTs). Therefore, assuming that the bulk deformability is reliably described by the elastic modulus E_{stone}, the joint closure $u_{j,n}$ can be expressed as:

$$u_{j,n} = u_{LVDT} - \frac{\sigma_n \cdot L_{LVDT}}{E_{stone}} \tag{3}$$

where L_{LVDT} is the specimen's height monitored by the LVDTs (Fig. 2c).

To investigate the specimens' behaviour both at high and low normal stress levels, this study utilises two different control protocols, namely force-controlled (FC) and displacement-controlled (DC). FC tests initiate with the actuator and the specimens already in contact and consist of five loading–unloading cycles reaching 1/3 of the material compressive strength (rounded to 16 MPa). Each cycle is composed of an incremental loading ramp of 1/5 of the total load and an unloading ramp that decreases the contact load to (around) 0.2 MPa, always ensuring contact. To capture lower (than 0.2 MPa) stress levels, this study also adopts DC tests, which are again composed of five loading–unloading cycles. However, each cycle is controlled independently and initiates and terminates with a gap between the actuator and the specimen, hence providing a detailed description of the joint behaviour at low stress levels. Overall, 10 different pairs of specimens are tested using both FC and DC protocols aiming to examine the variability of different contacting surfaces.

2.3.2. Shear-box tests

To evaluate the tangential properties of the dry-joint, this work employs the shear-box apparatus of Fig. 3 [63]. Its main constituents are (Fig. 3a-b): i) a drive unit imposing the horizontal displacement and the normal force, ii) a box containing the bottom specimen, iii) a metal frame bounding the top specimen, iv) two load cells placed both in the normal and tangential direction to measure the corresponding reaction forces, and v) a digital control panel to manage the tests. For the purposes of these tests, the examined squared (limestone) specimens have 58.5 mm (CoV = 1.5 %, N = 7) base-width and 27.7 mm (CoV = 13.1 %, N = 7) height (Fig. 3c). During each test, the two specimens in contact introduce a discontinuity that keeps the original limestone asperities. The specimens are precompressed with a constant normal stress σ_n, while they are sheared assuming a predefined displacement and constant velocity (0.1 mm/min). In total, 10 pairs of specimens are tested, each of them subjected to 20 normal stress levels ranging from 0.004 MPa to 1 MPa. This particular setup assumes that: i) the applied (constant) normal stress is uniformly distributed over the interface, ii) wear and debris accumulation of the surfaces after sequential testing are not significant, and iii) the specimens do not rotate in plan. The first assumption emerges due to the lever-arm created by the shearing forces,

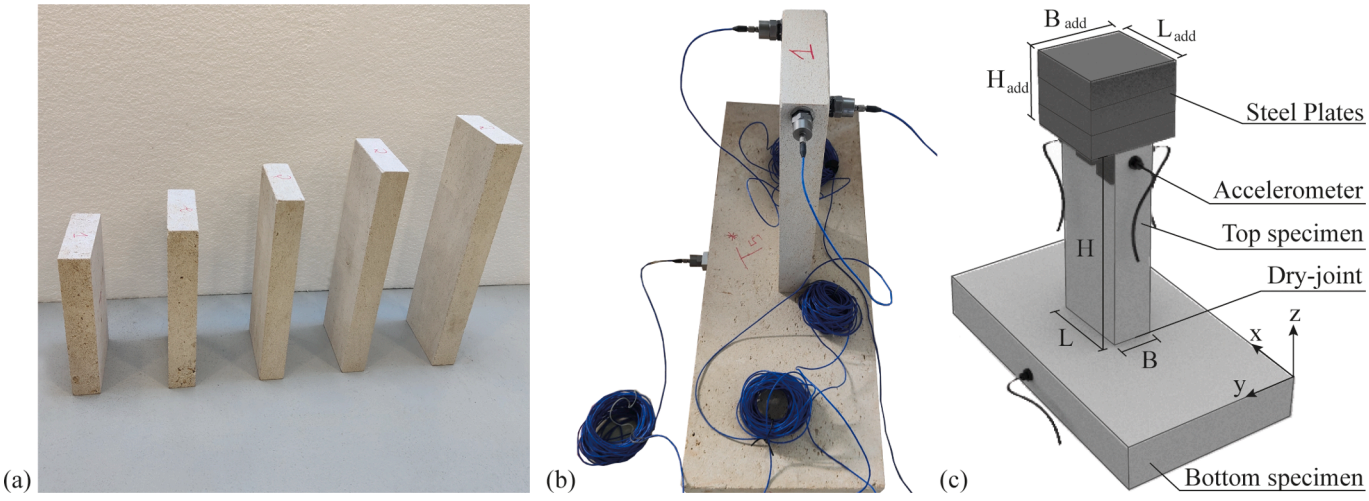

Fig. 4. (a) Limestone specimens of different height H and same base dimensions B, L, (b) vibration-based setup, and (c) schematic representation of a vibration-based test with additional steel plates.

which for the apparatus of Fig. 3b and the specimens' dimensions results in a (normalised over the width) eccentricity of less than 10 %, which does not jeopardise the reliability of the tests. Next, sequential testing may induce wear and debris accumulation [53,64]. However, no substantial debris was recorded, hence its influence is disregarded as a second assumption. Finally, the third assumption is that the specimens are placed without an initial misalignment introducing a rotation. This is acceptable given the repetitive nature of such experiments, which easily allows the identification and correction of potential errors via an outlier analysis.

Given that this work solely focuses on the interface properties, the interface relative displacement is locally measured with a Digital Image Correlation (DIC) system (Fig. 3a,d) [21,42,52,65], thus avoiding biased results arising from both the bulk deformability of the specimens and the flexibility of the apparatus [21].

2.4. Vibration-based approach

A vibration-based method is additionally considered to characterise the interface stiffness and interface damping of units in dry contact [66,67]. The vibration-based tests are conducted by placing a specimen on the ground and a free-standing specimen on top of the former, thus composing the interface under investigation (Fig. 4). The examined specimens are excited by the ambient noise of the laboratory, and hence the specimens experience vibrations of very low amplitude (perturbations), which permits the use of linear dynamics. This constitutes an essential detail of the method, as the dynamics of dry-joints are highly non-linear and non-negligible amplitudes do not allow the employment of linear dynamics when extracting modal properties [68]. Four piezoelectric accelerometers record the dynamic response of the specimens (Fig. 4b). Three of them are placed on the top extremities of the top specimen; two anti-diametrically positioned in the y-y direction and one in the x-x direction (Fig. 4b). Finally, one accelerometer is also placed on the bottom specimen to record the vibrations that are not related to the dry-joint (e.g. arising from the substructure's dynamic characteristics, or from any specific narrow-band noise of the laboratory). Finally, a sampling rate of 2000 Hz is employed for all tests, while the acquisition duration is 30 min.

This section adopts two different experimental setups to investigate the effect of both the normal stress and surface variability on the interface properties. The first is composed of five specimens with the same dimensions, i.e. $B = 49.3$ mm (CoV = 0.3 %, N = 5), $L = 151.0$ mm (CoV = 0.6 %, N = 5), $H = 398.6$ mm (CoV = 0.1 %, N = 5), with B, L and H being the dimensions of the top specimen gradually loaded with steel plates (Fig. 4c). The first steel plate is positioned on top of the free-standing specimen, and it is glued with two supporting L profiles to ensure sufficient connection. A total of nine steel plates (with a mass of 10.91 kg each) are sequentially placed on top of each other, reaching a maximum normal stress at the interface of 0.14 MPa. The second experimental setup investigates the surface variability by testing a large number of different in size specimens (in total 60), which have plan dimensions $B = 49.9$ mm (CoV = 1.7 % N = 60), $L = 150.8$ mm (CoV = 0.5 %, N = 60), while their height H varies from $H = 200$ mm to $H = 750$ mm with steps of 50 mm (Fig. 4a). This also allows more refined observations of the normal stress influence on the interface properties in the corresponding range, i.e. from 0.004 MPa to 0.016 MPa. Importanlty, for consistency, both setups keep the dimensions of the tested interfaces constant, while the variable height of the specimens is

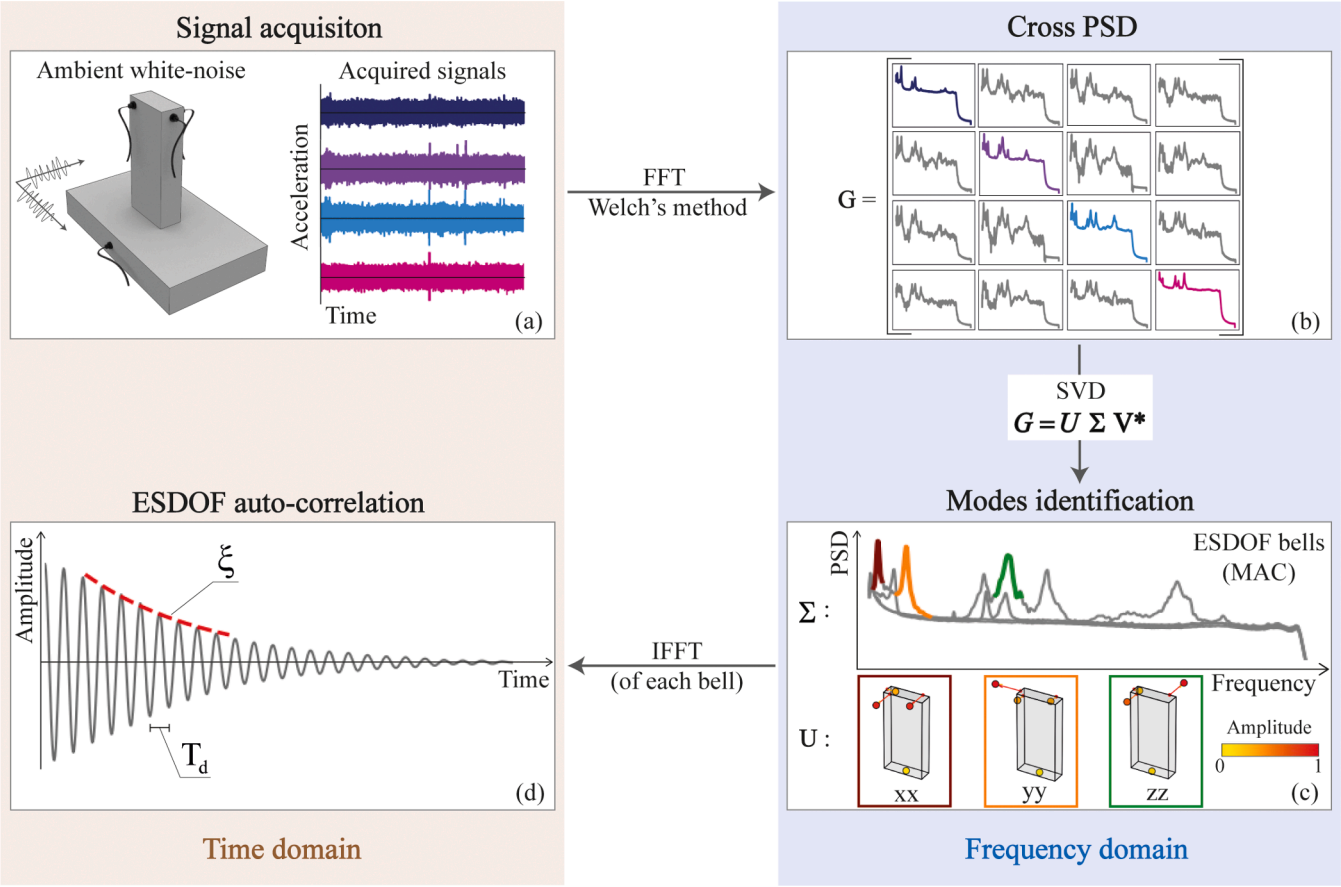

Fig. 5. Workflow of the Enhanced Frequency Domain Decomposition (EFDD) method: (a) signal acquisition under ambient white noise excitation, (b) Cross Power Spectral Density (CPSD) matrix using the Welch's method, (c) Singular Value Decomposition (SVD) of CPSD and modes identification (frequencies and mode shapes), and (d) autocorrelation of identified Equivalent Single Degree Of Freedom (ESDOF) modes using Inverse Fast Fourier Transformation (IFFT).

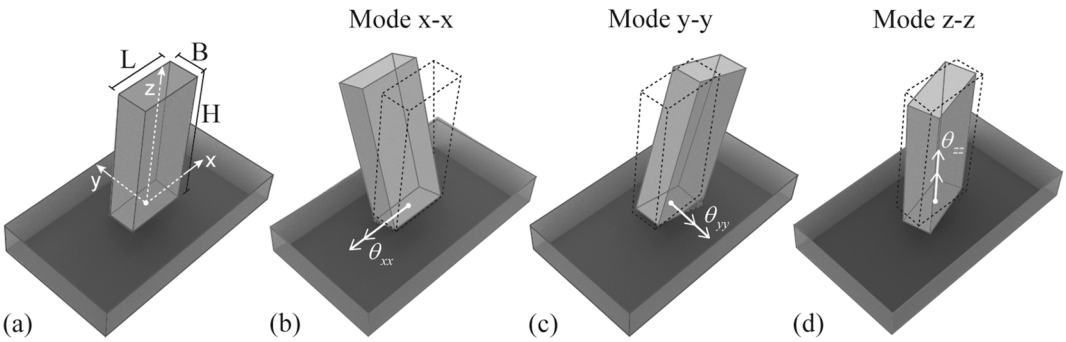

Fig. 6. (a) Adopted system for the vibration-based tests. Vibration mode shapes related solely to the interface stiffness: rotational over the (b) x-x, (c) y-y, and (d) z-z axes.

expected to be irrelevant for the localised properties of the interface (as it is the case when conducting joint-closure and shear-box tests). In both experimental setups, each specimen is tested on both sides (*LxB*), while the bottom specimen ($B = 270$ mm, $L = 720$ mm, $H = 90$ mm) is kept the same. Overall, 10 tests are performed both for each normal stress level of the first setup (i.e. varying the additional mass on top) and each height group of the second setup (i.e. varying the top specimen's height), resulting in a total of 210 vibration-based tests.

This work employs the Enhanced Frequency Domain Decomposition (EFDD) method [69,70] to estimate the dynamic properties (i.e. frequencies of vibration, mode shapes, and damping) of the system of Fig. 4. The EFDD is a well-known and widely used method [71], which primarily focuses on the frequency domain and comprises an output-only technique. Fig. 5 illustrates the workflow of the EFDD method, which assumes a zero-mean Gaussian white noise (herein the ambient noise of the laboratory) as the excitation of the system (Fig. 5a). The acquired (from the piezoelectric accelerometers) response signals are then used to construct the Cross Power-Spectral Density (CPSD) matrix G through the Fast Fourier Transform (FFT) after applying the Welch's method with overlapping time segments using Hanning windowing (Fig. 5b). Consequently, the singular value decomposition (SVD) is applied on the CPSD matrix ($G = U\Sigma V^*$, where, in general, U and V* are orthogonal complex unitary matrices, while Σ is a diagonal non-negative matrix which includes the singular values). This process, under certain assumptions (i.e. low damping and orthogonality of modes), results in spectral densities of Equivalent Single Degree Of Freedom (ESDOF) systems where the singular vectors U represent their corresponding experimental mode shapes (Fig. 5c). At this stage, the peak-picking technique is used on the spectral densities of the singular values Σ of Fig. 5c, accompanied by the phase and amplitude of their mode shapes U. Furthermore, the enhancement of the method suggests that the frequency intervals of the spectra Σ with similar vectors U correspond to the same ESDOF. These regions, commonly referred to as ESDOF "bells", are identified using the Modal Assurance Criterion (MAC) [72] on the vectors U (using a MAC threshold of 0.8). More importantly, these "bells" represent auto-correlation functions of the ESDOF when transformed back to the time domain using the Inverse Fast Fourier Transformation (IFFT) (Fig. 5d). Subsequently, the damped period $T_{damped,i}$ and damping ratio $\xi_{vibr,i}$ of each identified ESDOF are computed in the time domain using the well-established logarithmic decrement method (Fig. 5d) [59], where i refers to each identified mode. It is worth underlying that, to avoid biased results, the autocorrelation is divided by a triangular window, for which amplitudes larger than 0.85 and lower than 0.25 are disregarded during the damping estimation procedure [66]. Lastly, the natural frequencies $f_{natural,i}$ are simply calculated by combining the damped periods with the extracted damping ratios as [59]:

$$f_{natutal,i} = \frac{1}{T_{damped,i}\sqrt{1-\xi_{vibr,i}^2}} \tag{4}$$

Furthermore, the results of the EFDD method provide an estimation of the interface stiffness through the identification of the dynamic properties of the system (i.e. frequencies of vibration and mode shapes). Assuming rigidity of the examined bodies and complete fixity of the bottom specimen with the ground, this section provides a simplified analytical model to estimate both normal and tangential interface stiffness between the two (limestone) specimens. For completeness, Appendix A presents a more detailed numerical model, which also accounts for the interaction mechanism at the interfaces of the examined specimens with the ground and the steel plates, respectively, the interaction between the steel plates, and the bulk deformability of the bodies themselves (see e.g. Fig. A.1a in Appendix A). Under the rigidity (of the bodies) and fixity (of the bottom specimen with the ground) assumptions, three modes of vibration are identified for the top specimen (Fig. 6a): i) two rotational modes over the x-x (Fig. 6b) and y-y axes (Fig. 6c), which are related to the normal interface stiffness k_n, and ii) one rotational mode over the z-z axis (Fig. 6d), which is related to the tangential interface stiffness k_s. The corresponding generalised mass $M_{gen,i}$ and generalised stiffness $K_{gen,i}$ of each mode can be computed directly as the moment of inertia and second moment of area, respectively, as shown in Table 1, where m denotes the mass of the specimen (i.e. $m = \rho \cdot B \cdot L \cdot H$, with ρ being the material density). Note in Table 1 that the terms in brackets appear only when an additional mass m_{add} (here in the form of the steel plates of Fig. 4c) is placed on the top specimen, with B_{add}, L_{add} and H_{add} corresponding to the respective geometrical

Table 1
Generalised mass and generalised stiffness of the three rotational modes of Fig. 6.

Mode	M_{gen}	K_{gen}
rotational over the x-x axis	$m\left(\frac{1}{12}B^2+\frac{1}{3}H^2\right)+\left\{m_{add}\left(\frac{1}{12}\left(B_{add}^2+H_{add}^2\right)+\left(H+\frac{H_{add}}{2}\right)^2\right)\right\}$	$\frac{1}{12}k_nB^3L$
rotational over the y-y axis	$m\left(\frac{1}{12}L^2+\frac{1}{3}H^2\right)+\left\{m_{add}\left(\frac{1}{12}\left(L_{add}^2+H_{add}^2\right)+\left(H+\frac{H_{add}}{2}\right)^2\right)\right\}$	$\frac{1}{12}k_nBL^3$
rotational over the z-z axis	$\frac{1}{12}m(B^2+L^2)+\left\{\frac{1}{12}m_{add}\left(B_{add}^2+L_{add}^2\right)\right\}$	$\frac{1}{12}k_sBL(B^2+L^2)$

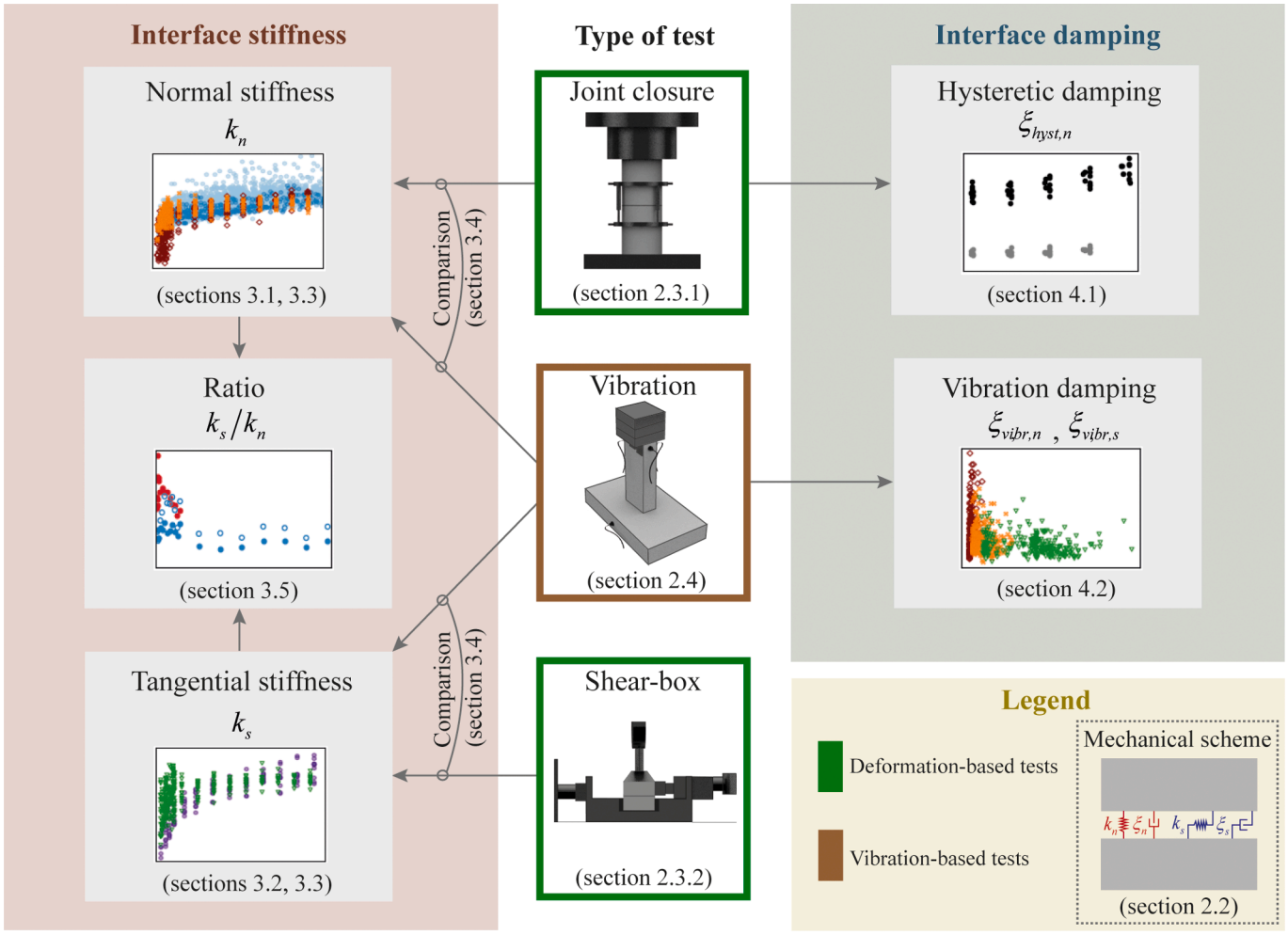

Fig. 7. Workflow of the experimental campaign.

dimensions of that mass (see e.g. Fig. 4c). Therefore, the normal and tangential interface stiffness are computed using Table 1 and Eq. (5):

$$K_{gen,i} = M_{gen,i} \cdot \left(2 \cdot \pi \cdot f_{natural,i}\right)^2 \tag{5}$$

Finally, the estimation of the vibration damping ratio ξ_{vibr} through the EFDD method relies on the time segments' length of the Welch's method (Fig. 5) [73]. In particular, relatively large time segments provide a higher frequency resolution, yet, with a noisy CPSD spectrum, while smaller time segments yield smoother CPSD spectrum with the cost of lower frequency resolution. To achieve a reliable estimation of the damping ratio, the present study adopts a convergence analysis strategy—similar to [71,74,75]—during which each test is iteratively analysed by increasing the time segment length until convergence of the damping ratio is achieved. Convergence is assumed when three consecutive estimations differ less than 20 %, while the time segment length is equal to 2^n data points and progressively increases with the integer $n \in [10, 19]$.

2.5. Experimental overview

Fig. 7 summarises the workflow of the experimental campaign and the main outcomes of the present study. Fig. 7 reveals the twofold aim of this investigation, which lies both in the quantification of the normal and tangential interface stiffness through joint closure (Section 3.1), shear-box (Section 3.2), and vibration-based tests (Section 3.3) and the energy dissipation of dry-joint interfaces in terms of hysteretic (Section 4.1) and vibration damping (Section 4.2). Importantly, this work also emphasises the comparison of the normal and tangential interface stiffness (Section 3.4) derived from the adopted experimental methodologies, i.e. deformation-based (Sections 3.1 and 3.2) and vibration-based (Section 3.3). The comparison reveals, for the first time, remarkable similarities and thus facilitates a more robust relationship between the normal and tangential interface stiffness (Section 3.5).

3. Interface stiffness

3.1. Deformation-based joint closure tests

Fig. 8a plots a representative joint closure loading–unloading cyclic response $u_{j,n}$ (Eq. (3)) with respect to the applied normal stress σ_n following the force-controlled (FC) methodology of Section 2.3.1. In particular, Fig. 8a shows a notable non-linear behaviour of the interface, characterised by low stiffness at low stress levels and very stiff behaviour at higher stress levels; in accordance with the literature [16,39,43]. From a physical perspective, the dry-joint interface stiffening stems from the gradual increase of the real-contact area of the micro-asperities [15,16,76,77]. At high stress levels, complete closure of the interface is almost achieved (here around 65 μm). Additionally, Fig. 8a reveals that inelastic deformations do occur, resulting in approximately 40 % of the residual displacement upon unloading. This is mainly attributed to the plastic deformation of the protruding asperities of the surface [16,39]. Fig. 8a clearly shows a distinct load path upon primitive loading, i.e. upon loading under normal stresses that had not been previously attained (e.g. A to B- (in red) or D to E (in orange) in Fig. 8a),

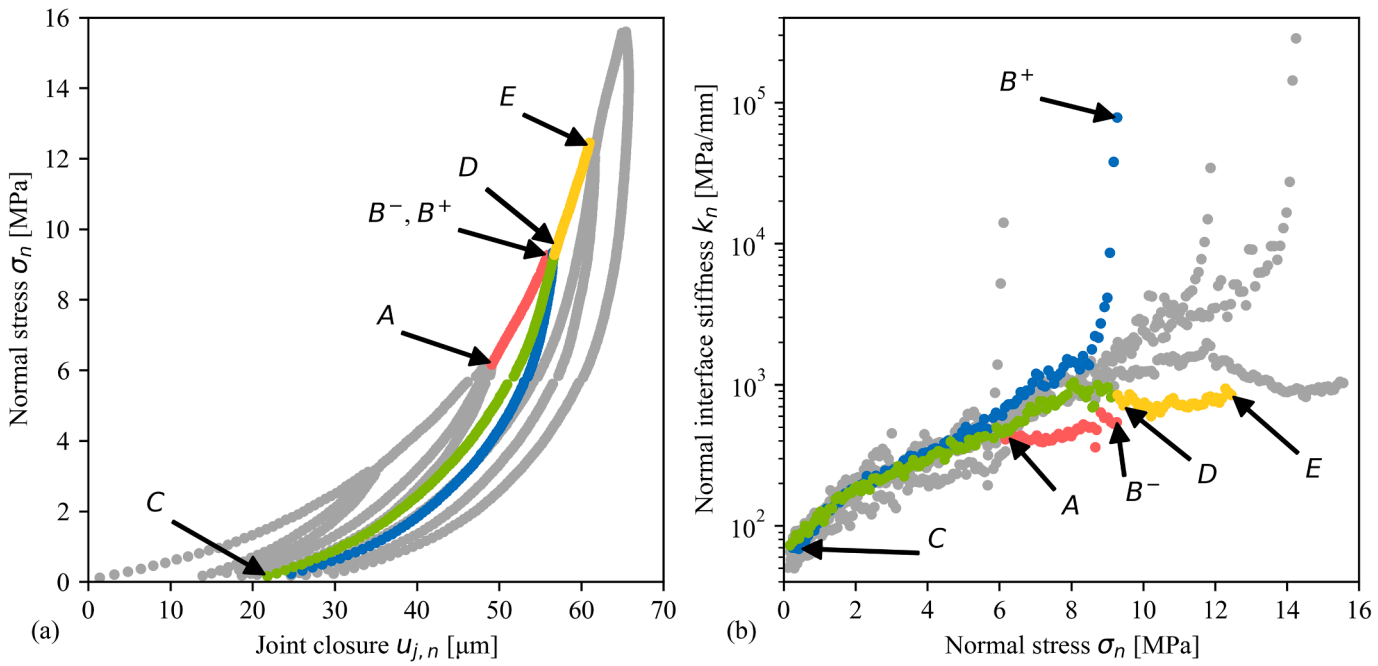

Fig. 8. (a) Representative joint closure response $u_{j,n}$ under loading–unloading cycles after a force-controlled (FC) test, and (b) the corresponding normal interface stiffness k_n.

and non-primitive loading (e.g. C to D (in green) in Fig. 8a) or unloading (e.g. B + to C (in blue) in Fig. 8a). Finally, unloading and reloading cycles in Fig. 8a display hysteresis, which may be associated with friction phenomena between the partially oblique asperities at the micro-scale upon joint closure/opening [78]. Note that such energy losses, stemming from both the plastic deformations and frictional hysteresis, are quantified in Section 4.

Fig. 8b illustrates the normal interface stiffness k_n derived from the interface response of Fig. 8a, calculated as the gradient of the normal stress over the joint closure (Eq. (1)), on logarithmic scale with respect to the acting normal stress σ_n. As anticipated, the normal interface stiffness displays low values (i.e. 50–100 MPa/mm) for normal stresses between 0.2 MPa and 1 MPa and notably high values (i.e. 1000–5000 MPa/mm) for normal stresses above 10 MPa. In addition, during the first primitive loading (e.g. A to B− in Fig. 8a or Fig. 8b), one can notice the relatively low stiffness of 400–500 MPa/mm (depicted in red in Fig. 8b), appearing as a lower bound. When loading reverses to unloading (e.g. B−, B+ in Fig. 8a), an abrupt hundredfold increase of the interface stiffness is apparent (e.g. B− to B+ in Fig. 8b), followed by a subsequent path (in blue) that progressively tends to coincide with the previous unloading and non-primitive loading stiffness data points. As expected, approaching zero stress-state (e.g. C in Fig. 8b), the normal interface

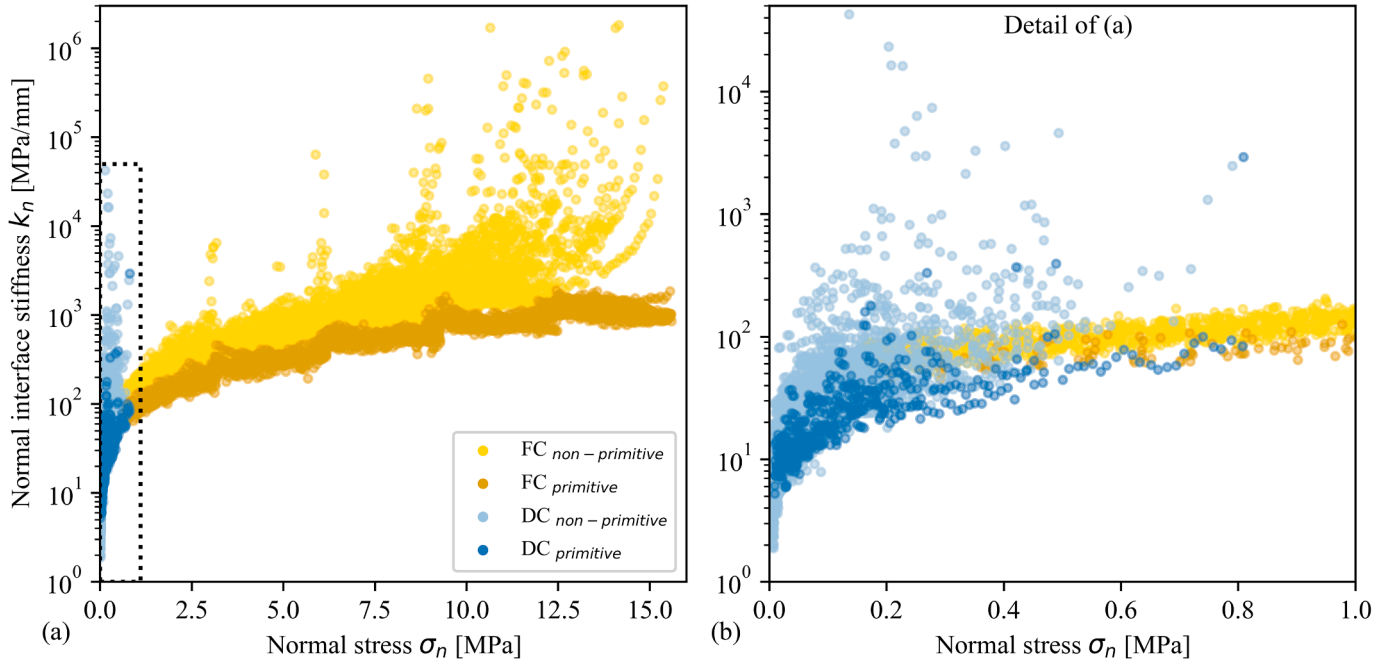

Fig. 9. (a) Normal interface stiffness k_n after all the displacement-controlled (DC) and force-controlled (FC) tests, respectively, and (b) detailed representation of Fig. 9a.

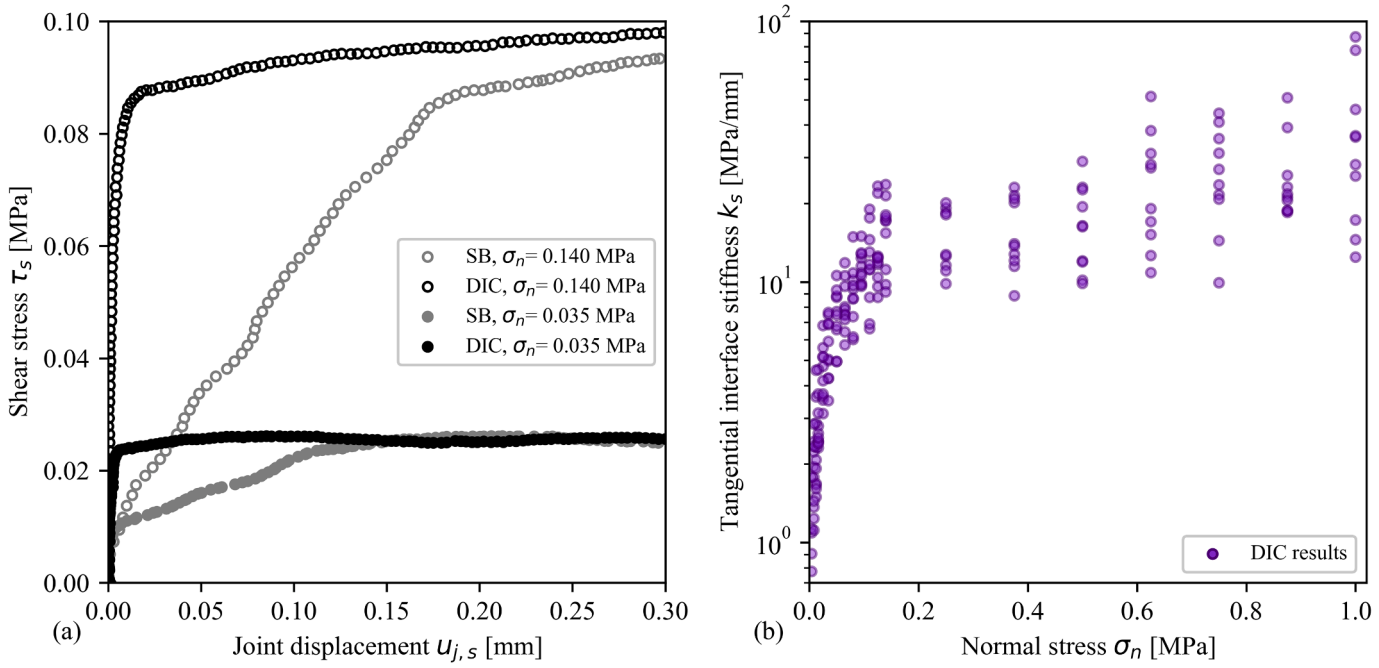

Fig. 10. (a) Representative shear-box test results for two different levels of pre-compression normal stress (i.e. $\sigma_n = 0.035$ MPa and $\sigma_n = 0.140$ MPa) using the Shear-Box (SB) and the Digital Image Correlation (DIC) system, and (b) tangential interface stiffness k_s with respect to the applied normal stress σ_n acquired from all the shear-box tests of Section 2.3.2 using the DIC acquisition system.

stiffness tends to zero. In turn, during non-primitive reloading (e.g. C to D (in green) in Fig. 8b), the interface stiffness closely follows the unloading path (in blue). Importantly, when the primitive stress-state is once more approached (e.g. D in Fig. 8b), the interface stiffness smoothly drops again from 1000 MPa/mm to 600 MPa/mm (e.g. D in Fig. 8b) back to the primitive loading path (e.g. up to E (in orange) in Fig. 8b).

Fig. 9 summarises the normal interface stiffness k_n estimations derived from all the joint closure tests performed herein, both after the FC and DC protocols explained in Section 2.3.1, corresponding respectively to high normal stress levels (i.e. from 0.2 MPa to 16 MPa) and low normal stress levels (i.e. from 0.005 MPa to around 0.8 MPa). Overall, the two testing procedures (i.e. FC and DC) present a similar behaviour of the normal interface stiffness, and importantly they show a satisfactory continuity between them. At first, Fig. 9a reveals a notable dispersion of the stiffness, partially attributed to the aleatory variability of the twenty different tested specimen interfaces. Specifically, in the FC tests (Fig. 9a) under non-primitive loading status, distinct normal stiffness spikes (up to 10^6 MPa/mm) appear due to the loading–unloading reverse (e.g. B + in Fig. 8b). Similar spikes (up to 10^4 MPa/mm) are also apparent in the DC tests (see detail in Fig. 9b), however, they are disorderly spread due to the experimental procedure followed (Section 2.3.1). In summary, despite the aforementioned dispersion, Fig. 9 clearly shows that as the normal stress σ_n increases, the normal interface stiffness k_n increases as well, while it tends to zero for very low stresses, i.e. when approaching separation. Moreover, as explained in detail in Fig. 8, the normal interface stiffness k_n follows two distinct paths depending on the loading history: i) lower stiffness values are observed upon primitive loading, while ii) higher stiffness values are shown upon unloading and/or non-primitive loading. Transitions between these two stiffness paths occur: i) with a discontinuous increase when reversing from primitive loading to unloading, and ii) with a smooth drop when approaching the primitive loading.

3.2. Deformation-based shear-box tests

This section presents the results of the shear-box tests of Section 2.3.2. Fig. 10a plots the tangential relative displacement $u_{j,s}$ with respect to the applied shear stress τ_s of two representative tests when the applied normal stress is equal to $\sigma_n = 0.035$ MPa and $\sigma_n = 0.140$ MPa. In addition, Fig. 10a compares the joint displacement $u_{j,s}$ acquired simultaneously by both the shear-box (SB) apparatus (i.e. using LVDTs) and the DIC system (see e.g. Fig. 3), and it reveals considerable inconsistency between the two results. More specifically, the flexibility of the whole shear-box apparatus, that the LVDTs inherently consider, leads to an unrealistic estimation of the tangential relative displacement and subsequently the tangential interface stiffness. In contrast, the DIC system seems to be a more reliable acquisition method (at least for the particular tests of the present study) as it directly measures the tangential relative displacement disregarding any influence of the testing apparatus. Nevertheless, Fig. 10a illustrates well-known aspects of dry-joint frictional behaviour [22,53]. Initially, the joint experiences an elastic-stick phase up to the attainment of the shear strength (i.e. the plateau in Fig. 10a) that leads to the subsequent gross-slip phase. The transition from the stick to the slip phase occurs with a gradual stiffness degradation due to micro-slipping phenomena taking place at the interface. It is worth noting that higher normal stress leads to a steeper slope (Fig. 10a), resulting in higher tangential interface stiffness k_s (Eq. (1)). This characteristic may be attributed to the larger area of contacting asperities at the micro-scale of the interface due to the higher normal stress [31,41,50].

Fig. 10b summarises the tangential interface stiffness k_s acquired from all the shear-box tests of Section 2.3.2 using the DIC system as the acquisition method, spanning from (around) 0.8 MPa/mm to 100 MPa/mm, with each data point corresponding to a single experiment. Due to the gradual influence of the micro-slipping phenomena (as shown in Fig. 10a), the tangential interface stiffness of each shear-box test is estimated from the initial 30 % of the shear strength [40,52]. The noted

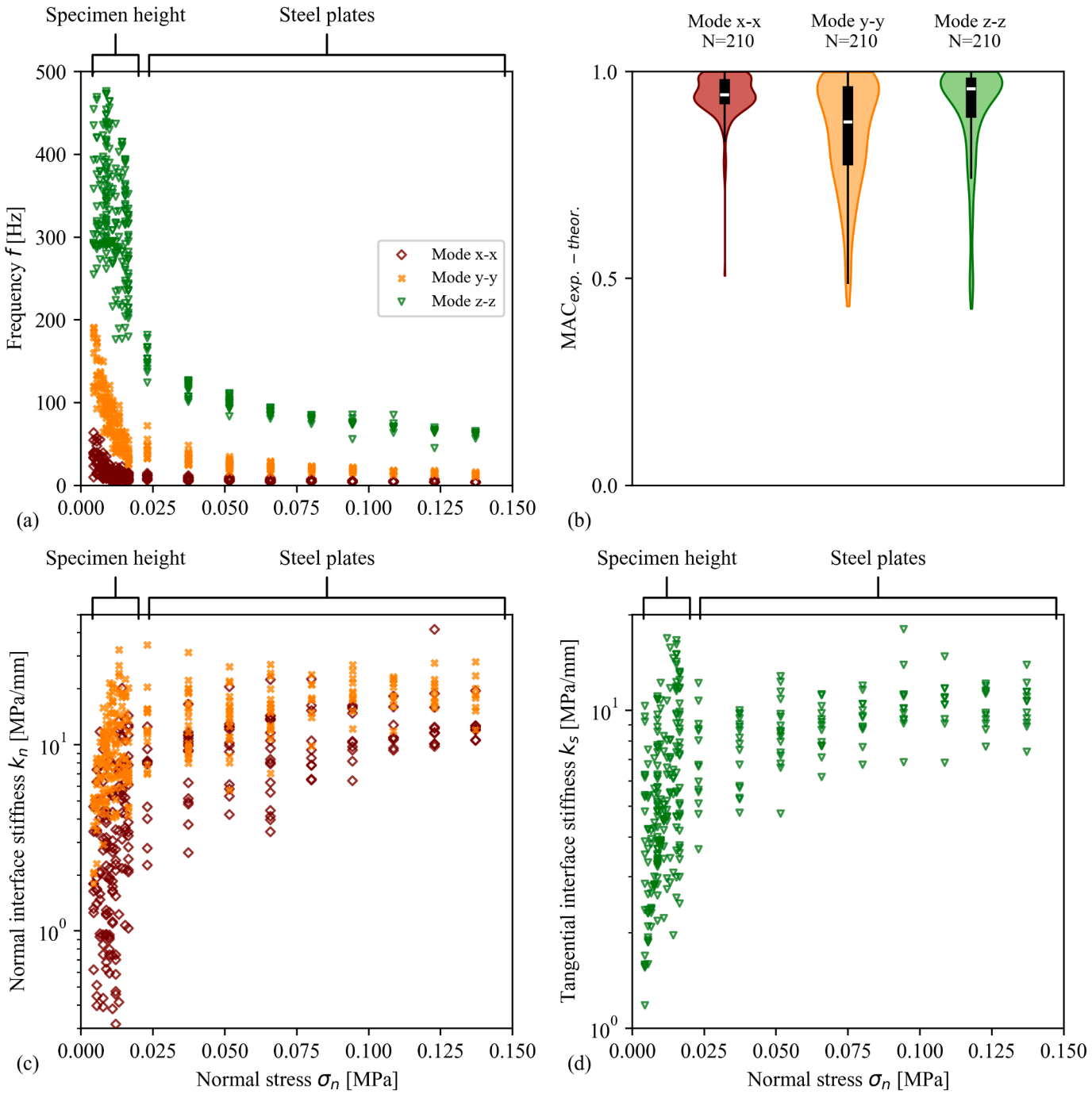

Fig. 11. Identified modal frequencies f with respect to the normal stress σ_n, (b) statistical distribution of the Modal Assurance Criterion (MAC) values, (c) normal (k_n) and (d) tangential (k_s) interface stiffness.

scatter for each normal stress level (Fig. 10b) stems from the aleatory variability of the surface of the tested specimens and their intrinsic irregularities [39]. Nevertheless, Fig. 10b is in agreement with past studies ([52] among others), illustrating that the tangential interface stiffness k_s increases with the applied normal stress σ_n.

3.3. Vibration-based tests

Fig. 11a presents the results of the identified modal frequencies f with respect to the normal stress σ_n acting on the interface after the vibration-based tests of Section 2.4. Fig. 11a also indicates the two different groups of tests conducted in Section 2.4, where firstly additional (on top) steel plates and secondly the variation of the specimens' height H are considered to investigate the effect of both normal stress and surface variability on the interface properties. For each normal stress level, the frequency of the rotational mode over the x-x axis precedes the pertinent mode over the y-y axis, which is in turn followed by the mode over the z-z axis. Note that the identified modal frequencies decrease as the specimen's mass (and consequently the acting normal stress) increases. Additionally, Fig. 11b plots the statistical distribution of the Modal Assurance Criterion (MAC) values, which compares the experimentally measured mode shapes with the idealised ones of Fig. 6. In general, the MAC takes values from null to unity; the closer to unity the better the agreement. Fig. 11b unveils the remarkable

concordance between the experimental and idealised mode shapes with MAC values very close to unity, thus validating the methodological assumptions of the present study.

Fig. 11c and Fig. 11d illustrate the normal and tangential interface stiffness, respectively, obtained by the experimentally measured modal frequencies of Fig. 11a. This is achieved using Table 1 and Eq. (5) for the modes over the x-x and y-y axes (Fig. 11c), while the mode over the z-z axis (Fig. 11d) is treated employing the detailed numerical model presented in Appendix A. This deliberate choice is based on the realisation that the bulk deformability of the limestone specimens has a notable impact on the dynamic characteristics of the mode over the z-z axis, while its influence becomes marginal on the pertinent characteristics of the modes over the x-x and y-y axes (see e.g. Fig. A2 in Appendix A). Thus, the analytical model of Section 2.4 provides an accurate estimation of the normal interface stiffness k_n, while the numerical model of Appendix A provides a more reliable estimation of the tangential interface stiffness k_s. Overall, Fig. 11c and Fig. 11d clarify that as the normal stress increases, so do the normal and tangential interface stiffness. More specifically, under low normal stresses (up to 0.02 MPa, which corresponds to the group of tests where the height of the specimens varies), the normal interface stiffness k_n shows a smaller scatter when estimated using the rotational mode over the y-y axis, rather than the x-x axis. This discrepancy might arise either from the higher sensitivity of the mode over the x-x axis on the geometrical variability of the joint (contact) area or from the accidental and infinitesimal small contact losses due to geometrical irregularities at the interface (see the meso-scale assumption of Section 2.2). On the contrary, the MAC values shown in Fig. 11b depict that the mode over the x-x axis is identified with more confidence, while the mode over the y-y axis contains higher variability. The latter issue presumably appears due to the use of just one accelerometer (DOF) for the identification of the mode over the y-y axis, contrary to the modes over the x-x and z-z axes, where two accelerometers (DOFs) are employed. Nevertheless, the two modes provide very similar results in terms of normal interface stiffness k_n estimations, especially for higher normal stress levels (i.e. for the group of additional steel plate tests).

3.4. Comparison of experimental methods in estimating the interface stiffness

The current work employs two fundamentally different experimental methods for estimating the normal and tangential interface stiffness, i.e. the deformation-based (Section 2.3) and the vibration-based method (Section 2.4). The former method imposes load (or deformation) on the tested interface and quantifies the stiffness as the gradient of stress over the joint displacement (Eq. (1)), while the latter method quantifies the stiffness through the vibration frequencies related to the interface (Eq. (5)).

Fig. 12 summarises the results of both experimental methods (presented in detail in Sections 3.1, 3.2 and 3.3). More specifically, Fig. 12a compares the normal interface stiffness k_n measured by both the deformation-based joint closure tests (Fig. 9b) and the vibration-based tests (obtained by the modal frequencies over the x-x and y-y axes of Fig. 11c). As a first approach, Fig. 12a reveals a very good agreement between the two methods, both in terms of estimated values of stiffness and normal stress dependency. Importantly, the vibration-based results appear to be in line with the joint closure test results under primitive loading, indicating that ambient noise vibration perturbations are related to the local loading stiffness [16,52]. Similarly, Fig. 12b compares the tangential interface stiffness k_s obtained by the deformation-based shear-box tests (Fig. 10b) and the vibration-based tests (through the modal frequencies over the z-z axis of Fig. 11d). Similarly, Fig. 12b illustrates a good match between the two methods in estimating the tangential interface stiffness, especially concerning its normal stress dependency. A slight mismatch is observed for low normal stress levels (up to 0.02 MPa), where the deformation-based results provide a lower bound of the tangential interface stiffness. Nevertheless, the vibration-based results at this range of normal stress comprise a high variation of tested surfaces (i.e. 120 in total); thus, such aleatory variabilities increase the experimental scatter.

In summary, despite the different concepts and assumptions behind the two experimental methods, an excellent agreement in terms of the estimated interface stiffness is achieved. To the best of the authors' knowledge, this is the first time that such methods have been successfully compared and cross-validated yielding remarkable similarities and

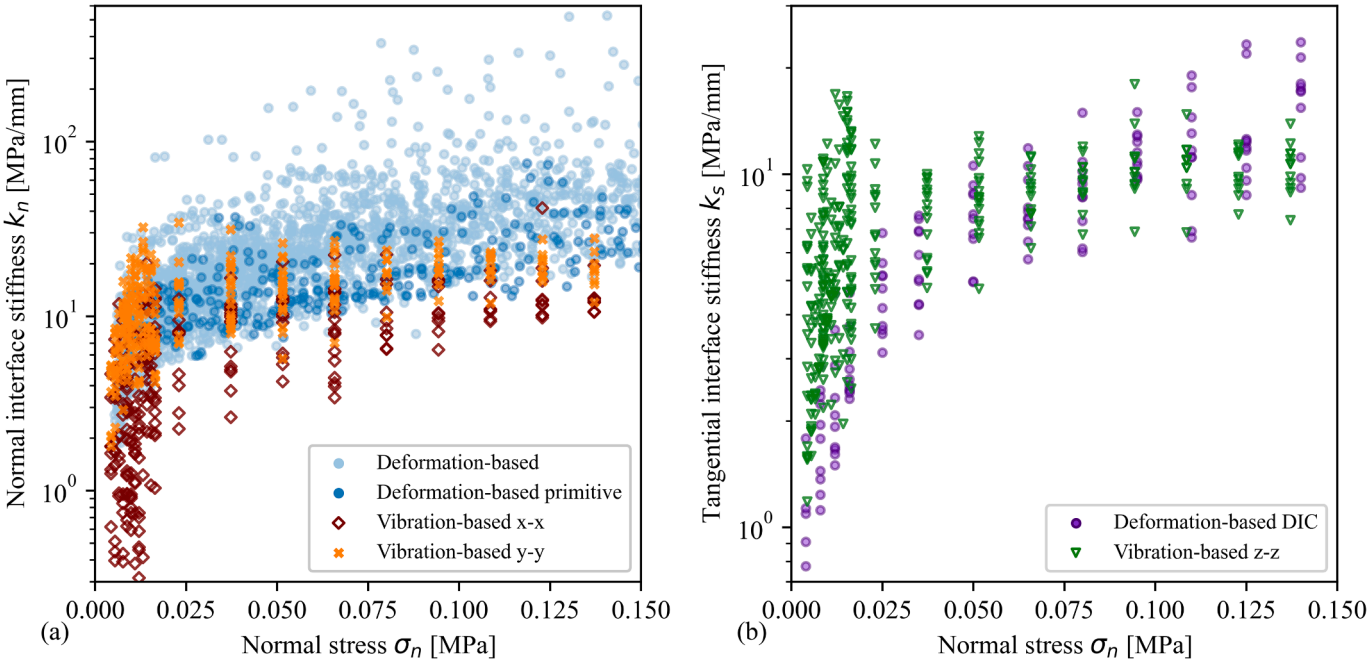

Fig. 12. Comparison of results between the deformation-based (Sections 3.1 and 3.2) and vibration-based methods (Section 3.3) for (a) the normal interface stiffness k_n, and (b) the tangential interface stiffness k_s with respect to the normal stress σ_n.

thus providing further reliability to the outcomes of the present experimental campaign. As a matter of fact, past attempts to compare different experimental methods for the estimation of the interface stiffness faced notable difficulties in obtaining comparable outcomes, possibly, among other reasons, due to the much stiffer interfaces tested [44,50,52].

3.5. Relationship between normal and tangential interface stiffness

Fig. 13a summarises the normal and tangential interface stiffness obtained by the vibration-based and the deformation-based tests. Each mark (in Fig. 13a) corresponds to the median stiffness value of the related normal stress level. Recall from Sections 2.4 and 3.3 that the vibration-based tests investigate a maximum normal stress of 0.14 MPa, while the deformation-based tests reach a maximum of 1 MPa (in this case limited by the shear-box apparatus). For the joint-closure tests, in particular, a distinction is made for the primitive loading results as Section 3.4 unveiled a closer match with the vibration-based method. Moreover, due to the larger amount of data collected for the non-primitive loading condition (stemming from the unloading and reloading paths after each cycle), the median values of all the data are closer to the non-primitive estimations. In general, Fig. 13a shows similar trends of interface stiffness between the two approaches highlighting again the reliability of the vibration-based tests against the deformation-based tests.

Fig. 13b plots the ratio of the tangential and normal interface stiffness k_s/k_n against the normal stress σ_n. In general, it shows high and scattered values of the stiffness ratio (i.e. $0.2 < k_s/k_n < 1.0$) for low normal stress levels (i.e. 0.004 MPa $< \sigma_n <$ 0.2 MPa), followed by a stabilisation of approximately $k_s/k_n = 0.3$ for $\sigma_n > 0.2$ MPa. More specifically, the primitive deformation-based results present higher values of the stiffness ratio (i.e. $0.3 < k_s/k_n < 0.6$) in comparison with all the data of the deformation-based tests that provide a lower bound estimation (i.e. $0.2 < k_s/k_n < 0.4$). Furthermore, the vibration-based method presents high values of the ratio k_s/k_n (i.e. $0.4 < k_s/k_n < 1.0$), thus showing a better agreement with the primitive deformation-based results. In summary, the interface stiffness ratio k_s/k_n demonstrates notable scatter for low normal stress levels, yet, it gradually reaches a plateau of around $k_s/k_n = 0.3$, indicating that k_n and k_s increase at similar rates. It is worth noting that this value of stiffness ratio lies within the range of $0.01 < k_s/k_n < 0.65$ reported by previous studies for a variety of different materials [31–33,39].

4. Interface damping

This section investigates in more detail the energy loss phenomena that occur at the interface (i.e. interface damping in Fig. 7). A distinction is made between the hysteretic and vibration damping estimations owing to their different origin. In particular, i) hysteretic damping is herein of static nature and arises due to relative displacements at the interface (in the order of 10^{-5} m), while ii) vibration damping is inherently dynamic and occurs under ambient noise vibration perturbations (in the order of 10^{-6} m).

4.1. Hysteretic damping

The hysteretic energy losses that occur at the interface become apparent through the force–displacement (or equivalently stress-displacement) response of the deformation-based tests of Fig. 8a and Fig. 10a. Frictional hysteretic energy losses (from shear-box tests) can be incorporated within a constitutive law in a straightforward manner [18,23]. On the contrary, joint closure tests show complex hysteretic behaviour upon loading/unloading (as described in Section 3.1), including both plastic interface deformations and frictional hysteresis loops due to the oblique asperities (see e.g. Fig. 8a) and merit further investigation. Thus, the aim of this section is to quantify solely the hysteretic damping from joint closure tests through the equivalent viscous damping approach [60].

In this context, Fig. 14a and Fig. 14c illustrate a representative joint closure loading–unloading cyclic test of the response $u_{j,n}$ with respect to the applied normal stress σ_n (similar to Fig. 8a). For clarity, only one cycle is presented. Fig. 14a and Fig. 14c indicate the dissipated (E_d) and stored (E_e) energies at the interface together with their simplified counterparts that a constitutive law could incorporate, i.e. Fig. 14b and

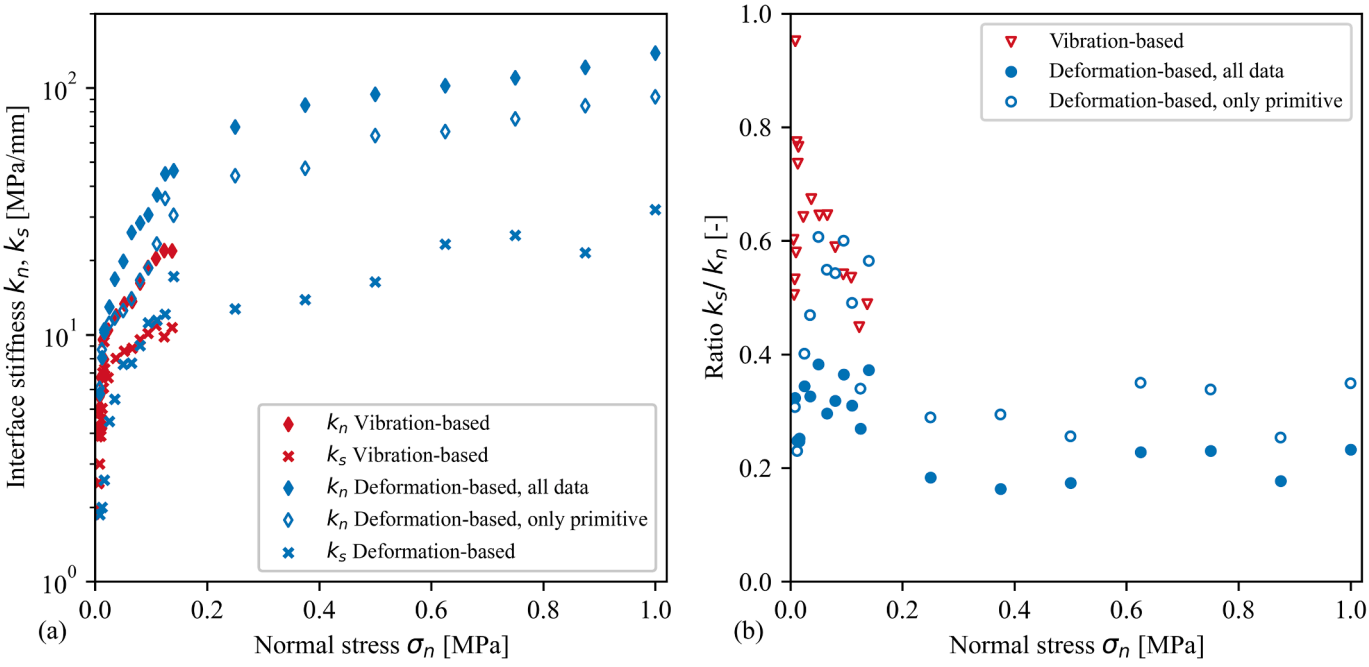

Fig. 13. (a) Comparison of normal k_n and tangential k_s interface stiffness median values and (b) k_s/k_n ratio obtained by the vibration-based and deformation-based tests.

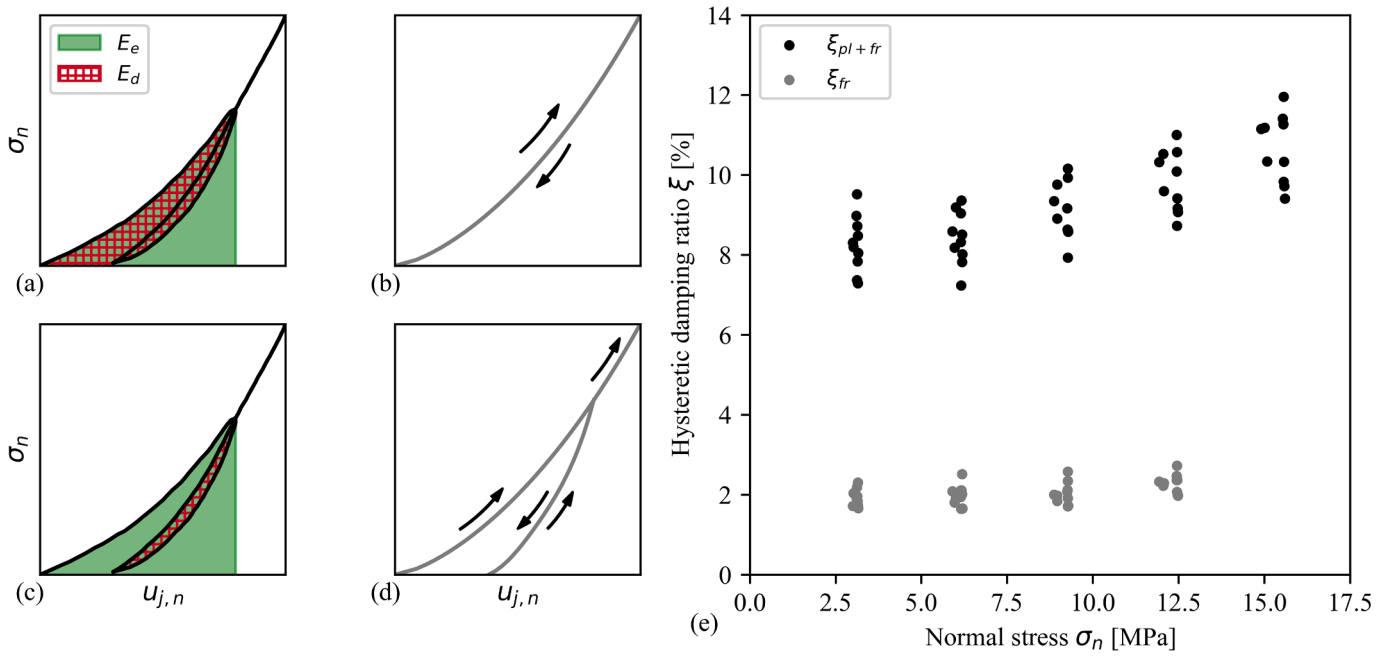

Fig. 14. (a, c) Stored (E_e) and dissipated (E_d) energy of simplified constitutive laws, which disregard either (b) the plastic and frictional energy losses, or (d) solely the frictional energy losses. (e) Hysteretic equivalent damping ratios from the deformation-based tests of Section 3.1.

Fig. 14d, respectively. In particular, Fig. 14a, and subsequently Fig. 14b, consider the total hysteretic energy losses due to plastic deformations and friction at the interface, while Fig. 14c, and subsequently Fig. 14d, consider the hysteretic energy losses due to friction solely.

Using the experimental outcomes of all the deformation-based joint closure tests of Section 3.1 and through Eq. (2), Fig. 14e plots both the hysteretic damping ratios representative of the energy losses due to i) friction $\xi_{hyst,n,fr}$ and ii) plastic deformation and friction (combined) $\xi_{hyst,n,pl+fr}$, against the normal stress σ_n. For the purposes of Fig. 14e, the hysteretic damping ratios are computed at four different stress levels (i.e. $\sigma_n \approx$ 3.2, 6.3, 9.5, 12.6 MPa), which correspond to the unloading–reloading cycles of the joint closure tests (Section 3.1). Additionally, the last unloading of the tests allows only the calculation of the hysteretic damping ratio $\xi_{hyst,n,pl+fr}$ at $\sigma_n \approx$ 15.8 MPa, since reloading is not performed. Fig. 14e illustrates that the hysteretic damping ratio $\xi_{hyst,n,pl+fr}$ is, on average, five times larger than $\xi_{hyst,n,fr}$. Specifically, the former indicates a notable damping ratio between 7.2 % $< \xi_{hyst,n,pl+fr} <$ 12 %, while the latter varies between 1.6 % $< \xi_{hyst,n,fr} <$ 2.8 %. Moreover, the frictional hysteretic damping ratio $\xi_{hyst,n,fr}$ gives a rather constant

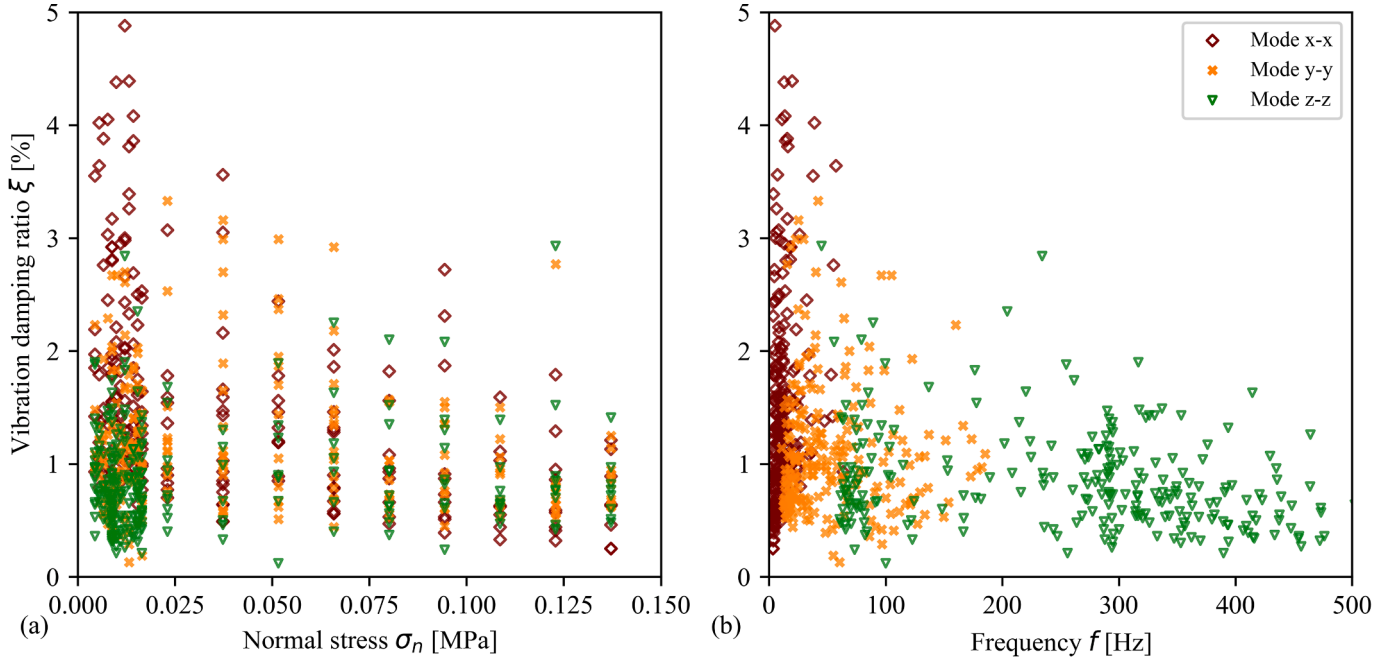

Fig. 15. Vibration damping ratio of all the identified modes from the vibration-based tests of Section 2.4 with respect to the (a) interface normal stress σ_n, and (b) frequency f.

value at different normal stress levels, while the coupled plastic and frictional hysteretic damping ratio $\xi_{hyst,n,pl+fr}$ shows an increasing trend with the normal stress. This growing tendency possibly stems from the plastic component of the hysteretic energy losses. Finally, note that, in case of $\xi_{hyst,n,pl+fr}$, decoupling the plastic energy loss from the frictional loss is infeasible since they appear concurrently. Similarly, $\xi_{hyst,n,fr}$ cannot be extracted from $\xi_{hyst,n,pl+fr}$, as $\xi_{hyst,n,fr}$ includes frictional losses during non-primitive loading conditions, while $\xi_{hyst,n,pl+fr}$ refers solely to primitive loading conditions.

4.2. Vibration damping

The application of the EFDD method (Fig. 5) on the results of the vibration-based tests of Section 2.4 facilitates the estimation of the vibration damping at the interface. This estimation is associated with the interface damping $\xi_{vibr,n}$ and $\xi_{vibr,s}$, as the identified modes are related to the interface. Fig. 15 summarises the vibration damping ratios plotted against the interface normal stress σ_n (Fig. 15a) and the identified modal frequencies f (Fig. 15b). Recall that the estimations of the modes over the x-x and y-y axes correspond to the damping ratio acting in the normal direction of the interface (see ξ_n in Fig. 1b), while the mode over the z-z axis represents the damping ratio acting in the tangential direction of the interface (see ξ_s in Fig. 1b). As a first approach, Fig. 15 depicts a relatively weak correlation of the damping ratio with both the normal stress and frequency, and a rather constant value of around 1 %. In addition, Fig. 15 reveals a higher scatter of the damping ratios at lower normal stress and frequency levels. More specifically, the mode over the x-x axis presents the highest scatter with damping ratios up to (almost) 5 %, while the modes over the y-y and z-z axes provide less dispersed results, namely up to 3 %. It is worth mentioning that such scatter on the damping ratio estimation is expected due to the inherent sensitivity of the EFDD method to noisy signals, such as the ambient noise of the laboratory used herein. In this context, Magalhães et al. [71] underlined that even with an improved signal, i.e. with less noise, variation in damping ratio estimations is still present. Overall, the results of all the vibration modes appear to conjoin notably well, indicating the presence of a constant damping ratio, equal for both the normal and tangential directions of the dry-joint interface.

5. Discussion and conclusions

This work presents a meso-scale experimental campaign on the interface properties of dry-joint limestone specimens with the aim of quantifying the interface stiffness and interface damping. To this end, two fundamentally different experimental methods are employed and cross-validated, namely deformation-based and vibration-based. These methods estimate the interface properties through either measurement of the stress-deformation response or quantification of the dynamic characteristics (i.e. frequencies of vibration, mode shapes, and damping ratio) of the examined structural system. Even though the experimental campaign on limestone specimens provides *ad hoc* outcomes, it, most importantly, provides a general methodology that can be adopted for the mechanical characterisation of the dry-joint contact interface of any masonry-like material.

This study confirms that the interface stiffness increases with the normal stress acting at the interface, while it tends to zero when approaching separation. This behaviour is attributed to the gradual increase of the real-contact area of the micro-asperities, which affects both the normal and tangential responses. In more detail, the joint closure tests show a marked non-linear trend in the response, where the primitive normal loading is characterised by lower normal interface stiffness in comparison with unloading or non-primitive loading conditions. In addition, shearing the dry-joint shows phases of sticking, micro-slipping and gross-slipping, with the tangential interface stiffness better estimated at the initial part of the sticking phase. Finally, the ratio of the tangential over the normal interface stiffness illustrates scattered values at low normal stress levels, while a constant value of (around) 0.3 governs higher normal stress levels. In general, this study reveals that despite their conceptual differences, the two experimental methods (i.e. deformation-based and vibration-based) show an excellent agreement in estimating the interface stiffness, highlighting their ability to serve as independent predictors of the interface properties.

Given the agreement between the two methods, their experimental requirements and capabilities may play a decisive role. As a first approach, the deformation-based tests, namely joint closure and shear-box tests, are performed in a straightforward manner using typical laboratory equipment. Joint closure tests require a reaction frame, actuator, and LVDTs, while shear-box tests require the standard shear-box apparatus or any equivalent laboratory setup together with a localised measurement of the joint relative displacement (e.g. using a DIC system). On the other hand, vibration-based tests require only a few accelerometers and a data acquisition system, thus giving the possibility to be also performed under in-situ conditions. In addition, the deformation-based method requires two different test setups for characterising both the normal and tangential interface stiffness (i.e. joint closure and shear-box tests), while the vibration-based method provides both parameters concurrently.

Finally, the present work identifies two distinct types of energy dissipation that occur at the interface (i.e. hysteretic and vibration) assuming an equivalent viscous damping representation. Hysteretic energy losses are observed after the joint closure tests and are associated with inelastic deformations and hysteresis upon unloading–reloading cycles. On the other hand, vibration damping shows a relatively constant damping ratio for both the normal and tangential directions of the interface. It is apparent that a characterisation of the interface damping in full should consider both sources of dissipation and thus perform both types of tests.

In conclusion, this work presents an extensive experimental characterisation campaign of dry-joint masonry structures. The current study employs conceptually different experimental techniques and provides a critical appraisal and indicative guidelines on their use and outcomes. Overall, such a plethora of collected experimental data paves the way for the formulation of reliable constitutive laws of dry-joint interfaces. This constitutes a crucial step toward the simulation of the complex non-linear dynamic behaviour of dry-joint masonry structures since, to the best of the authors' knowledge, such experimental data is missing from the literature.

CRediT authorship contribution statement

Georgios Vlachakis: Conceptualization, Data curation, Investigation, Methodology, Software, Validation, Visualization, Writing – original draft, Writing – review & editing. **Carla Colombo:** Conceptualization, Data curation, Investigation, Methodology, Software, Validation, Visualization, Writing – original draft, Writing – review & editing. **Anastasios I. Giouvanidis:** Investigation, Methodology, Supervision, Writing – original draft, Writing – review & editing. **Nathanaël Savalle:** Investigation, Methodology, Supervision, Writing – original draft, Writing – review & editing. **Paulo B. Lourenço:** Funding acquisition, Resources, Supervision, Writing – review & editing.

Declaration of Competing Interest

The authors declare the following financial interests/personal relationships which may be considered as potential competing interests: Paulo B. Lourenço is a member of the Editorial Advisory Board of the Journal of Construction and Building Materials.

Data availability

Data will be made available on request.

Acknowledgements

This work has been partly financed by FCT/MCTES through national funds (PIDDAC) under the R&D Unit Institute for Sustainability and Innovation in Structural Engineering (ISISE), under reference UIDB/04029/2020. This work is financed by national funds through FCT – Foundation for Science and Technology, under grant agreements 2020.07325.BD and PRT/BD/152830/2021 attributed to the first and second authors, respectively. This study has been partly funded by the STAND4HERITAGE project (new STANDards FOR seismic assessment of built cultural HERITAGE) that has received funding from the European Research Council (ERC) under the European Union's Horizon 2020 research and innovation program (Grant No. 833123) as an Advanced Grant. The opinions and conclusions presented in this paper are those of the authors and do not necessarily reflect the views of the sponsoring organisations. The authors also greatly acknowledge the technical support from the staff of the University of Minho laboratory during the experimental campaign, and Dr Alberto Barontini from the University of Minho for the fruitful discussions and comments related to the vibration-based tests.

Appendix A. Influence of different sources of flexibility on the estimation of the interface stiffness via vibration-based tests

This section presents a detailed investigation of the influence of different sources of flexibility of the experimental setup of Section 2.4 on the estimation of the normal and tangential interface stiffness obtained by vibration-based tests. More specifically, besides the interface between the examined limestone specimens, the experimental setup of Section 2.4 is characterised by additional flexibilities, i.e. due to the interaction mechanism at the interfaces of the specimens with the ground and the steel plates, the interaction between the steel plates, and the bulk deformability of the bodies themselves (Fig. A.1a). To this end, this Section formulates a detailed finite element (FE) model (using the commercial software DIANA FEA [79]) which takes into account the aforementioned sources of flexibility.

Recall that Section 2.4 and Table 1 presume that the only source of flexibility is the interface stiffness between the two limestone specimens. Consequently, this implies that the influence of the bulk deformability of the bodies is negligible, while the rest of the interaction mechanisms are considered (theoretically) infinitely stiff. This is a simplification in an attempt to propose an easy-to-use method able to reliably estimate the interface stiffness between contacting bodies. In this context, this section investigates the accuracy of such an assumption and its impact on the interface stiffness estimation.

A.1. Description of the flexible numerical model

As shown in Fig. A.1a and Fig. A.1b, the flexible numerical model replicates the exact geometry of the experimental setup of Fig. 4 using hexahedral elements. It includes: i) the bottom specimen laying on the ground, ii) the free-standing top specimen, and iii) the steel plates placed on top of the free-standing specimen. Furthermore, finite stiffness is assigned at the interfaces between: a) the bottom specimen and the (fixed) ground, i.e. stone-to-ground ($k_{n,stone-ground}$, $k_{s,stone-ground}$), b) the bottom specimen and the top specimen, i.e. stone-to-stone ($k_{n,stone-stone}$, $k_{s,stone-stone}$), c) the top specimen and the lower steel plate, i.e. stone-to-steel ($k_{n,stone-steel}$, $k_{s,stone-steel}$), and d) the steel plates, i.e. steel-to-steel ($k_{n,steel-steel}$, $k_{s,steel-steel}$). Note that all the interfaces are modelled with zero-thickness interface elements.

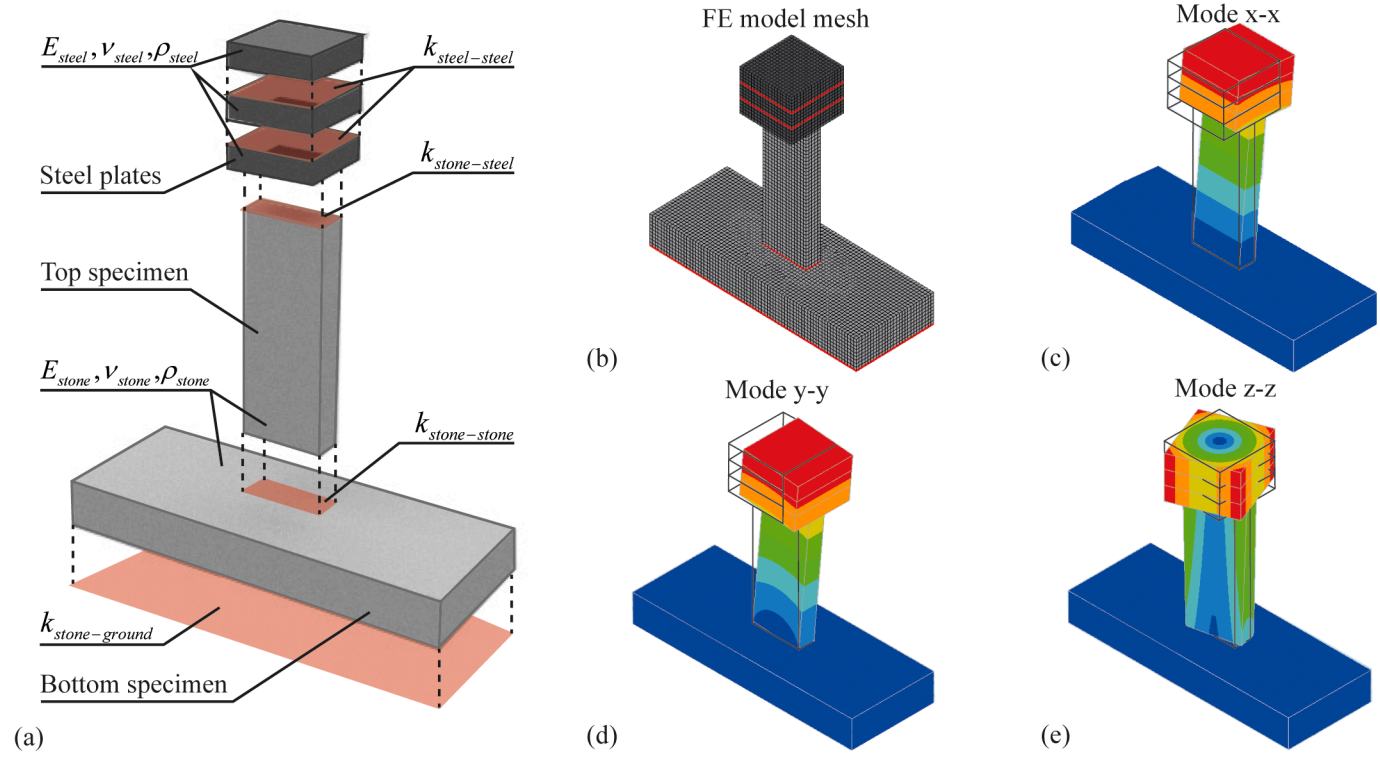

Fig. A.1. Representative flexible numerical model of the vibration-based tests: (a) schematic representation of the main components and parameters (b) FE model mesh, mode shapes over the (c) x-x, (d) y-y, and (e) z-z axes.

Table A.1
Mechanical properties adopted for the flexible numerical model.

Element	Parameter	Reference	Range
limestone specimens	Elastic modulus E_{stone} [GPa]	32.7	29.6–35.8
	Poisson's ratio ν_{stone} [–]	0.2	0.1–0.3
stone-to-stone interface	Normal stiffness $k_{n,stone-stone}$ [MPa/mm]	calibrated	2–40
	Tangential stiffness $k_{s,stone-stone}$ [MPa/mm]	calibrated	1–20
stone-to-steel interface	Normal stiffness $k_{n,stone-steel}$ [MPa/mm]	$1{\cdot}10^3$	$0.5–10{\cdot}10^3$
	Tangential stiffness $k_{s,stone-steel}$ [MPa/mm]	$5{\cdot}10^2$	$2.5–50{\cdot}10^2$
steel-to-steel interface	Normal stiffness $k_{n,steel-steel}$ [MPa/mm]	$1{\cdot}10^5$	$0.5–10{\cdot}10^5$
	Tangential stiffness $k_{s,steel-steel}$ [MPa/mm]	$5{\cdot}10^4$	$2.5–50{\cdot}10^4$
stone-to-ground interface	Normal stiffness $k_{n,stone-ground}$ [MPa/mm]	$1{\cdot}10^3$	$0.5–10{\cdot}10^3$
	Tangential stiffness $k_{s,stone-ground}$ [MPa/mm]	$5{\cdot}10^2$	$2.5–50{\cdot}10^2$

Table A.1 summarises the mechanical properties assigned to the flexible numerical model of Fig. A.1. A reference value characterises each parameter, while a range of values accounts for the epistemic uncertainty. More specifically, the elastic modulus E_{stone} and density $\rho_{stone} = 2238$ kg/m^3 of the limestone specimens have been experimentally characterised in Section 2.1. To investigate potential influence of E_{stone}, it is assigned herein with a variability equal to $\pm$ 2 times the experimentally derived standard deviation. The reference value and the range of values of the Poisson's ratio ν_{stone} are obtained by literature [80], while the properties of the steel plates are deterministically defined, with elastic modulus $E_{steel} = 200$ GPa, Poisson's ratio $\nu_{steel} = 0.2$ and density $\rho_{steel} = 7480$ kg/m^3. Regarding the interface properties that govern the interaction of the contacting bodies of the system of Fig. A1a, the reference and range of values of the steel-to-steel interface stiffness are collected from literature [16,31,41,42,45,47,49,50], while due to the lack of reliable estimations, the stone-to-steel and stone-to-ground interface stiffness are set as an intermediate order of magnitude between the stone-to-stone and steel-to-steel interface stiffness. Finally, the stone-to-stone interface stiffness is the unknown parameter of this investigation and therefore its value is estimated by the flexible numerical model after interpolation of the experimental frequencies on the stiffness-frequency numerical results.

The (low amplitude) ambient noise vibrations of the experimental setup (Section 2.4) permit the use of linear dynamics and thus the flexible numerical model is examined using eigenvalue analysis. Furthermore, the flexible numerical model (Fig. A.1) and the rigid analytical model (Fig. 6 and Table 1) are compared in terms of vibration frequencies, which are obtained after eigenvalue analysis and use of Table 1 and Eq. (5), respectively, through the following error metric:

$$Error_f = \frac{f_{ANA} - f_{NUM}}{f_{NUM}} \tag{A.1}$$

where f_{NUM} and f_{ANA} are the vibration frequencies of the flexible numerical and rigid analytical models, respectively.

A.2. Error quantification on the interface stiffness estimation: flexible numerical model versus rigid analytical model

Fig. A.2 plots the error in the prediction of the vibration frequencies (Eq. (A.1)) between the flexible numerical model (Fig. A.1) and the rigid analytical model (Fig. 6 and Table 1), for the three identified modes of vibration with respect to the normal/tangential stiffness at the interface between the two (limestone) specimens for different normal stress levels. Fig. A.2 shows that as the interface stiffness increases, so does the error between the two models. This is attributed to the competing role between the stone-to-stone interface stiffness and the rest of the flexibilities on the dynamic characteristics of the flexible numerical model of Fig. A.1. Indeed, a rather flexible stone-to-stone interface governs the overall dynamics, and subsequently, the stiffness estimations between the rigid analytical model and the flexible numerical model are similar, hence providing negligible

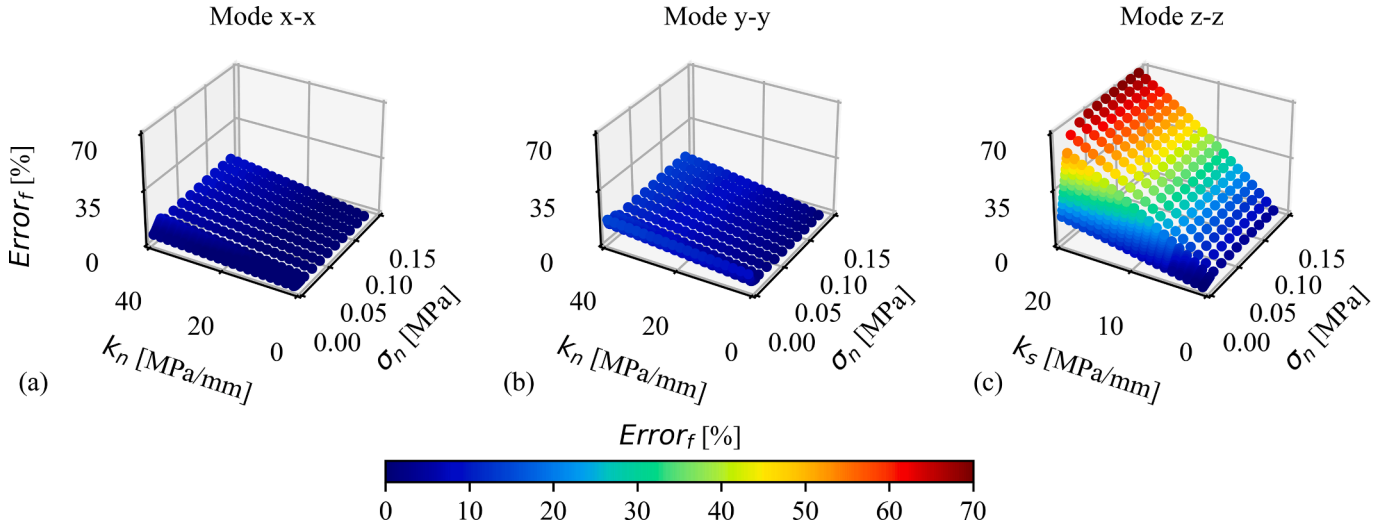

Fig. A.2. Error in the prediction of the frequencies (Eq. (A.1)) between the flexible numerical (Fig. A.1) and the rigid analytical model (Table 1) of the vibration-based tests, for the modes over (a) x-x, (b) y-y, and (c) z-z axes.

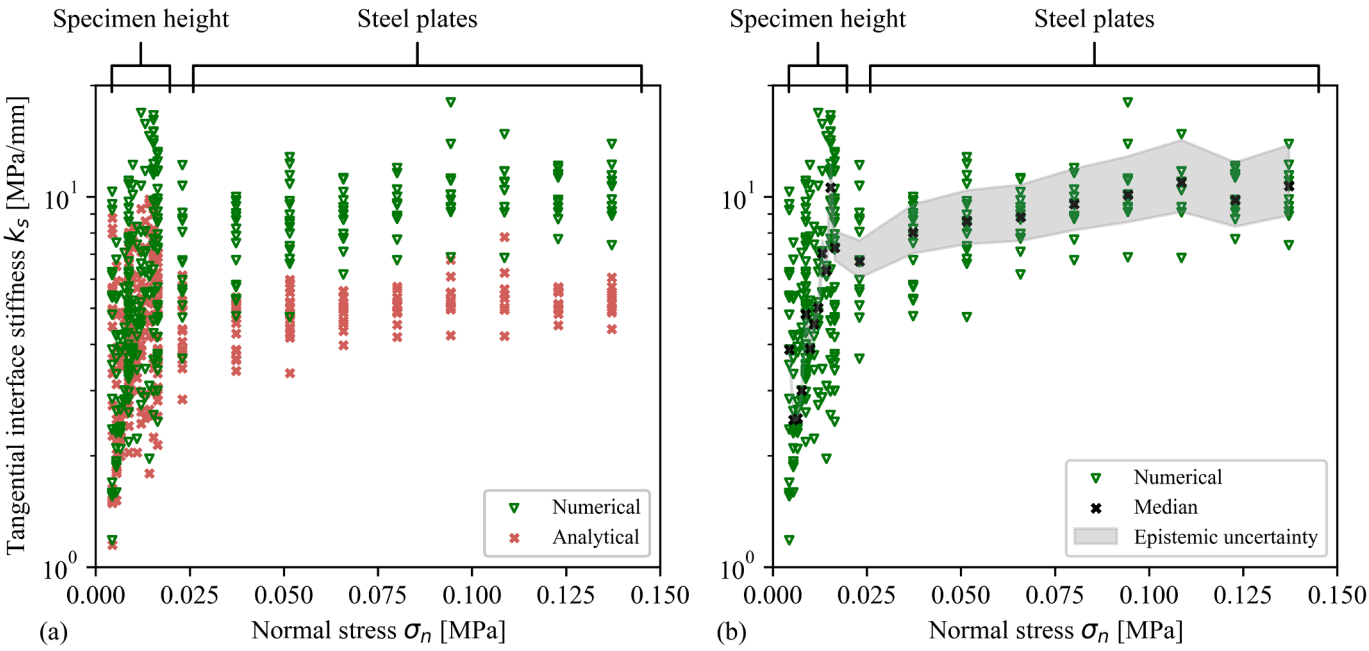

Fig. A.3. Tangential interface stiffness k_s estimation (a) using the flexible numerical (Fig. A.1) and the rigid analytical models (Table 1), and (b) influence of the epistemic uncertainty of the numerical model on the median values of the reference parameters (Table A.1).

error. On the contrary, the higher the stone-to-stone interface stiffness is, the lower its influence on the overall dynamics compared to the other sources of flexibility, therefore causing an increase in the error between the two models. Moreover, Fig. A.2 reveals that the error is minor (up to 16 %) for the modes over the x-x and y-y axes, while it substantially increases (up to 70 %) for the mode over the z-z axis. This observation implies that the rigidity assumption of the examined specimens presumed by the rigid analytical model is satisfactory for the first two modes (i.e. x-x and y-y), while it becomes inadequate for the mode over the z-z axis. Hence, the estimations of the normal interface stiffness k_n are reliable enough through the rigid analytical model of Section 2.4. On the contrary, a more reliable estimation of the tangential interface stiffness k_s can be obtained by the flexible numerical model. Finally, it is worth highlighting that a sensitivity analysis, the results of which are omitted herein for brevity, showed that the main source of this error stems from the bulk deformability of the top specimen (i.e. E_{stone} and ν_{stone}), while the rest of the parameters have a minor role. Subsequently, one can conclude that the influence of the specimen's bulk deformability is negligible for the normal interface stiffness k_n estimations, while it becomes substantial for the tangential interface stiffness k_s estimations. Thus, the rest of the current section focuses on the tangential interface stiffness.

Fig. A.3a compares the tangential interface stiffness k_s estimations obtained by both the flexible numerical model of Fig. A.1 and the rigid analytical model of Section 2.4. Fig. A.3a illustrates the considerable difference between the stiffness estimations of the two models, with the flexible numerical model providing a higher tangential interface stiffness k_s than the rigid analytical model. As expected, this is attributed to the different sources of flexibility the flexible numerical model considers while the rigid analytical model disregards. Finally, Fig. A.3b quantifies the influence of the epistemic uncertainty of the mechanical properties of Table A.1 on the tangential stiffness. To this end, the flexible numerical model is independently investigated under both the more flexible and stiffer bounds of the range of values of each parameter of Table A.1, e.g. lower bound of the various sources of flexibility and higher bound of the Poisson's ratio yield a more flexible numerical model. For the sake of this comparison, the stone-to-stone interface assumes the median experimental value depicted in Fig. A.3b. Fig. A.3b indicates that the more flexible bound provides a higher estimation of the tangential interface stiffness, while the stiffer bound provides a lower estimation of the tangential interface stiffness. In addition, Fig. A.3b illustrates that the epistemic uncertainty of the flexible numerical model remains within the aleatory variability of the experimental tests. More specifically, concerning the variation of height of the specimens, the epistemic uncertainty is significantly lower than the scatter of the experimental data, due to the aleatory uncertainties of the different 120 tested surfaces. On the other hand, the flexibility of the experimental setup becomes important for the groups of specimens tested with additional steel plates on top. Yet, only 10 different surfaces are tested for this group, resulting in smaller experimental scatter. In conclusion, Fig. A.3b reveals that the epistemic uncertainty of the numerical model does not undermine the estimation of the tangential interface stiffness k_s.

References

[1] P. Roca, P.B. Lourenço, A. Gaetani, Historic Construction and Conservation: Materials, Systems and Damage, Routledge Taylor & Francis Group, New York, 2019, https://doi.org/10.1201/9780429052767. ISBN 9781032090238.
[2] C. Colombo, N. Savalle, A. Mehrotra, M.F. Funari, P.B. Lourenço, Experimental, numerical and analytical investigations of masonry corners: Influence of the horizontal pseudo-static load orientation, Constr. Build. Mater. 344 (2022), https://doi.org/10.1016/j.conbuildmat.2022.127969.
[3] L.F. Restrepo Vélez, G. Magenes, M.C. Griffith, Dry stone masonry walls in bending-Part I: Static tests, Int. J. Archit. Herit. 8 (2014) 1–28, https://doi.org/10.1080/15583058.2012.663059.
[4] N. Bianchini, N. Mendes, C. Calderini, P.X. Candeias, M. Rossi, P.B. Lourenço, Seismic response of a small-scale masonry groin vault: experimental investigation by performing quasi-static and shake table tests, Bull. Earthq. Eng. 20 (2022) 1739–1765, https://doi.org/10.1007/s10518-021-01280-0.
[5] P.B. Lourenço, D.V. Oliveira, P. Roca, A. Orduña, Dry joint stone masonry walls subjected to in-plane combined loading, J. Struct. Eng. 131 (2005) 1665–1673, https://doi.org/10.1061/(ASCE)0733-9445(2005)131:11(1665).
[6] D. Bigoni, G. Noselli, Localized stress percolation through dry masonry walls. Part I - Experiments, Eur. J. Mech. / A Solids. 29 (2010) 291–298, https://doi.org/10.1016/j.euromechsol.2009.10.009.
[7] P.B. Lourenço, L.F. Ramos, Characterization of cyclic behavior of dry masonry joints, J. Struct. Eng. 130 (2004) 779–786, https://doi.org/10.1061/(ASCE)0733-9445(2004)130:5(779).

[8] G. Vasconcelos, P.B. Lourenço, Experimental characterization of stone masonry in shear and compression, Constr. Build. Mater. 23 (2009) 3337–3345, https://doi.org/10.1016/j.conbuildmat.2009.06.045.

[9] C.E. Barroso, D.V. Oliveira, L.F. Ramos, Physical and mechanical characterization of vernacular dry stone heritage materials: Schist and granite from Northwest Portugal, Constr. Build. Mater. 259 (2020), https://doi.org/10.1016/j.conbuildmat.2020.119705.

[10] A. Mehrotra, M.J. Dejong, A methodology to account for interface flexibility and crushing effects in multi-block masonry collapse mechanisms, Meccanica. 55 (2020) 1237–1261, https://doi.org/10.1007/s11012-020-01161-x.

[11] A.I. Vakis, V.A. Yastrebov, J. Scheibert, L. Nicola, D. Dini, C. Minfray, M. Ciavarella, Tribology International Modeling and simulation in tribology across scales : An overview, Tribol. Int. 125 (2018) 169–199, https://doi.org/10.1016/j.triboint.2018.02.005.

[12] J. Alves, N. Peixinho, M. Tavares, P. Flores, H.M. Lankarani, A comparative study of the viscoelastic constitutive models for frictionless contact interfaces in solids, Mech. Mach. Theory. 85 (2015) 172–188, https://doi.org/10.1016/j.mechmachtheory.2014.11.020.

[13] S. Natsiavas, Analytical Modeling of Discrete Mechanical Systems Involving Contact, Impact, and Friction, Appl. Mech. Rev. 71 (2019) 1–25, https://doi.org/10.1115/1.4044549.

[14] P. Flores, Contact mechanics for dynamical systems : a comprehensive review, Multibody Syst. Dyn. 54 (2021) 127–177, https://doi.org/10.1007/s11044-021-09803-y.

[15] J.A. Greenwood, J.B.P. Williamson, Contact of Nominally Flat Surfaces, Proc. R. Soc. Lond. A. Math. Phys. Sci. 295 (1966) 300–319, https://doi.org/10.1098/rspa.1966.0242.

[16] J. Kim, A. Baltazar, S. Rokhlin, Ultrasonic assessment of rough surface contact between solids from elastoplastic loading – unloading hysteresis cycle, J. Mech. Phys. Solids. 52 (2004) 1911–1934, https://doi.org/10.1016/j.jmps.2004.01.006.

[17] F. Marques, P. Flores, J.C.P. Claro, H.M. Lankarani, A survey and comparison of several friction force models for dynamic analysis of multibody mechanical systems, Nonlinear Dyn. 86 (2016) 1407–1443, https://doi.org/10.1007/s11071-016-2999-3.

[18] S. Medina, D. Nowell, D. Dini, Analytical and Numerical Models for Tangential Stiffness of Rough Elastic Contacts, Tribol. Lett. 49 (2013) 103–115, https://doi.org/10.1007/s11249-012-0049-y.

[19] B. Brogliato, Nonsmooth Mechanics: Models, Dynamics and Control, Communicat, Spring Verlag London Ltd. (1999), https://doi.org/10.1007/978-1-4471-0557-2.

[20] C. Casapulla, F. Portioli, Experimental and analytical investigation on the frictional contact behavior of 3D masonry block assemblages, Constr. Build. Mater. 78 (2015) 126–143, https://doi.org/10.1016/j.conbuildmat.2014.12.100.

[21] M.E. Kartal, D.M. Mulvihill, D. Nowell, D.A. Hills, Determination of the Frictional Properties of Titanium and Nickel Alloys Using the Digital Image Correlation Method, Exp. Mech. 51 (2011) 359–371, https://doi.org/10.1007/s11340-010-9366-y.

[22] B.N.J. Persson, Sliding Friction: Physical Principles and Applications, Spring-Verlag Berlin Heidelberg GmbH, 2000. ISBN-10 3540671927, https://link.springer.com/book/10.1007/978-3-662-04283-0.

[23] J. Wojewoda, A. Stefanski, M. Wiercigroch, T. Kapitaniak, Hysteretic effects of dry friction: modelling and experimental studies, Philos. Trans. R. Soc. A Math. Phys. Eng. Sci. 366 (2008) 747–765, https://doi.org/10.1098/rsta.2007.2125.

[24] M. ElGawady, Q. Ma, J. Butterworth, J. Ingham, Effects of interface material on the performance of free rocking blocks, Earthq. Eng. Struct. Dyn. 40 (2011) 375–392, https://doi.org/10.1002/eqe.1025.

[25] F. Galvez, L. Sorrentino, D. Dizhur, J.M. Ingham, Damping considerations for rocking block dynamics using the discrete element method, Earthq. Eng. Struct. Dyn. 51 (2022) 935–957, https://doi.org/10.1002/eqe.3598.

[26] J. Kim, F. Lorenzoni, M. Salvalaggio, M. Rosa, Seismic vulnerability assessment of free-standing massive masonry columns by the 3D Discrete Element Method, Eng. Struct. 246 (2021), 113004, https://doi.org/10.1016/j.engstruct.2021.113004.

[27] O. Al Shawa, G. De Felice, A. Mauro, L. Sorrentino, Out-of-plane seismic behaviour of rocking masonry walls, Earthq. Eng. Struct. Dyn. 41 (2012) 949–968, https://doi.org/10.1002/eqe.1168.

[28] P.D. Spanos, A. Di Matteo, A. Pirrotta, M. Di Paola, Rocking of rigid block on nonlinear flexible foundation, Int. J. Non. Linear. Mech. 94 (2017) 362–374, https://doi.org/10.1016/j.ijnonlinmec.2017.06.005.

[29] G. Vlachakis, A.I. Giouvanidis, A. Mehrotra, P.B. Lourenço, Numerical block-based simulation of rocking structures using a novel universal viscous damping model, J. Eng. Mech. 147 (2021) 04021089, https://doi.org/10.1061/(ASCE)EM.1943-7889.0001985.

[30] J.V. Lemos, Discrete Element Modeling of Masonry Structures, Int. J. Archit. Herit. 1 (2007) 190–213, https://doi.org/10.1080/15583050601176868.

[31] M. Gonzalez-Valadez, A. Baltazar, R.S. Dwyer-joyce, Study of interfacial stiffness ratio of a rough surface in contact using a spring model, Wear. 268 (2010) 373–379, https://doi.org/10.1016/j.wear.2009.08.022.

[32] S. Biwa, S. Hiraiwa, E. Matsumoto, Stiffness evaluation of contacting surfaces by bulk and interface waves, Ultrasonics. 47 (2007) 123–129, https://doi.org/10.1016/j.ultras.2007.08.005.

[33] G. Starzynski, R. Buczkowski, Ultrasonic Measurements of Contact Stiffness Between Rough Surfaces, J. Tribol. 136 (2014), https://doi.org/10.1115/1.4027132.

[34] T.T. Bui, A. Limam, V. Sarhosis, M. Hjiaj, Discrete element modelling of the in-plane and out-of-plane behaviour of dry-joint masonry wall constructions, Eng. Struct. 136 (2017) 277–294, https://doi.org/10.1016/j.engstruct.2017.01.020.

[35] B. Pulatsu, E.M. Bretas, P.B. Lourenço, Discrete element modeling of masonry structures : Validation and application, Earthquakes Struct 11 (2016) 563–582, https://doi.org/10.12989/eas.2016.11.4.563.

[36] P. Meriggi, G. de Felice, S. De Santis, F. Gobbin, A. Mordanova, B. Pantò, Distinct Element Modelling of Masonry Walls under Out-Of-Plane Seismic Loading, Int. J. Archit. Herit. 13 (2019) 1110–1123, https://doi.org/10.1080/15583058.2019.1615152.

[37] K. Papadopoulos, E. Vintzileou, I.N. Psycharis, Finite element analysis of the seismic response of ancient columns, Earthq. Eng. Struct. Dyn. 48 (2019) 1432–1450, https://doi.org/10.1002/eqe.3207.

[38] M.F. Vassiliou, M. Broccardo, C. Cengiz, M. Dietz, L. Dihoru, S. Gunay, K. M. Mosalam, G. Mylonakis, A. Sextos, B. Stojadinovic, Shake table testing of a rocking podium : Results of a blind prediction contest, Earthq. Eng. Struct. Dyn. 50 (2021) 1043–1062, https://doi.org/10.1002/eqe.3386.

[39] S. Bandis, A.C. Lumsden, N.R. Barton, Fundamentals of Rock Joint Deformation, Int. J. Rock Mech. Min. Sci. Geomech. Abstr. 20 (1983) 249–268, https://doi.org/10.1016/0148-9062(83)90595-8.

[40] P. Berthoud, T. Baumberger, Shear stiffness of a solid-solid multicontact interface, Proc. R. Soc. A Math, Phys. Eng. Sci. 454 (1998) 1615–1634, https://doi.org/10.1098/rspa.1998.0223.

[41] S. Filippi, A. Akay, M.M. Gola, Measurement of Tangential Contact Hysteresis During Microslip, J. Tribol. 126 (2004) 482–489, https://doi.org/10.1115/1.1692030.

[42] M.E. Kartal, D.M. Mulvihill, D. Nowell, D.A. Hills, Measurements of pressure and area dependent tangential contact stiffness between rough surfaces using digital image correlation, Tribol. Int. 44 (2011) 1188–1198, https://doi.org/10.1016/j.triboint.2011.05.025.

[43] P.H.S.W. Kulatilake, S. Shreedharan, T. Sherizadeh, B. Shu, Y. Xing, P. He, Laboratory Estimation of Rock Joint Stiffness and Frictional Parameters, Geotech. Geol. Eng. 34 (2016) 1723–1735, https://doi.org/10.1007/s10706-016-9984-y.

[44] V. Gimpl, A. Fantetti, S.W.B. Klaassen, C.W. Schwingshackl, D.J. Rixen, Contact stiffness of jointed interfaces : A comparison of dynamic substructuring techniques with frictional hysteresis measurements, Mech. Syst. Signal Process. 171 (2022), 108896, https://doi.org/10.1016/j.ymssp.2022.108896.

[45] X. Shi, A.A. Polycarpou, Measurement and Modeling of Normal Contact Stiffness and Contact Damping at the Meso, J. Vib. Acoust. 127 (2005) 52–60, https://doi.org/10.1115/1.1857920.

[46] G. Zhao, Z. Xiong, X. Jin, L. Hou, W. Gao, Prediction of contact stiffness in bolted interface with natural frequency experiment and FE analysis, Tribol. Int. 127 (2018) 157–164, https://doi.org/10.1016/j.triboint.2018.05.044.

[47] A. Baltazar, S.I. Rokhlin, C. Pecorari, On the relationship between ultrasonic and micromechanical properties of contacting rough surfaces 50 (2002) 1397–1416, https://doi.org/10.1016/S0022-5096(01)00119-3.

[48] B.W. Drinkwater, R.S. Dwyer-Joyce, P. Cawley, A Study of the Interaction between Ultrasound and a Partially Contacting Solid-Solid Interface, Proc. R. Soc. London. Ser. A Math. Phys. Eng. Sci. 452 (1996) 2613–2628, https://doi.org/10.1098/rspa.1996.0139.

[49] R.S. Dwyer-Joyce, B.W. Drinkwater, A.M. Quinn, The use of ultrasound in the investigation of rough surface interfaces, J. Tribol. 123 (2001) 8–16, https://doi.org/10.1115/1.1330740.

[50] A. Fantetti, S. Mariani, L. Pesaresi, D. Nowell, F. Cegla, C. Schwingshackl, Ultrasonic monitoring of friction contacts during shear vibration cycles, Mech. Syst. Signal Process. 161 (2021), 107966, https://doi.org/10.1016/j.ymssp.2021.107966.

[51] K. Kendall, D. Tabor, An ultrasonic Study of the Area of Contact between Stationary and Sliding Surfaces, Proc. R. Soc. A Math. Phys. Eng. Sci. 323 (1971) 321–340, https://doi.org/10.1098/rspa.1971.0108.

[52] D.M. Mulvihill, H. Brunskill, M.E. Kartal, R.S. Dwyer-joyce, D. Nowell, A Comparison of Contact Stiffness Measurements Obtained by the Digital Image Correlation and Ultrasound Techniques, Exp. Mech. (2013) 1245–1263, https://doi.org/10.1007/s11340-013-9718-5.

[53] A. Fantetti, L.R. Tamatam, M. Volvert, I. Lawal, L. Liu, L. Salles, M.R.W. Brake, C. W. Schwingshackl, D. Nowell, The impact of fretting wear on structural dynamics: Experiment and Simulation, Tribiology Int. 138 (2019) 111–124, https://doi.org/10.1016/j.triboint.2019.05.023.

[54] Les Pierres de Frontenac Website, (n.d.). http://www.pierres-frontenac.com/ (accessed July 30, 2022).

[55] H. Lovon, V. Silva, R. Vicente, T.M. Ferreira, A.A. Costa, Characterisation of the masonry building stock in Portugal for earthquake risk assessment, Eng. Struct. 233 (2021), https://doi.org/10.1016/j.engstruct.2021.111857.

[56] I. Rodríguez Pérez, G. Vasconcelos, P.B. Lourenço, P. Quintana, C. García, A. Dionísio, Physical-mechanical characterization of limestones from Yucatan churches, Mexico, J. Build. Eng. 44 (2021), https://doi.org/10.1016/j.jobe.2021.102895.

[57] G. Pappalardo, S. Mineo, C. Monaco, Geotechnical characterization of limestones employed for the reconstruction of a UNESCO world heritage Baroque monument in southeastern Sicily (Italy), Eng. Geol. 212 (2016) 86–97, https://doi.org/10.1016/j.enggeo.2016.08.004.

[58] ASTM D7012-14E1. Standard Test Methods for Compressive Strength and Elastic Moduli of Intact Rock Core Specimens under Varying States of Stress and Temperatures, 2017, https://doi.org/10.1520/D7012-14E01.

[59] A.K. Chopra, Dynamics of Structures: Theory and Applications to Earthquake Engineering 13 (2023), ISBN-13: 9780137848737. https://www.pearson.com/en-us/subject-catalog/p/dynamics-of-structures-theory-and-applications-to-earthquake-engineering/P200000003471?view=educator.

[60] L. Jacobsen, Damping in composite structures, in: Proc. 2nd World Conf. Earthq. Eng., Tokyo, 1960: pp. 1029–1045.
[61] C.A. Blandon, M.J.N. Priestley, Equivalent viscous damping equations for direct displacement based design, J. Earthq. Eng. 9 (2005) 257–278, https://doi.org/10.1142/S1363246905002390.
[62] M.J.N. Priestley, D.N. Grant, Viscous damping in seismic design and analysis, J. Earthq. Eng. 9 (2005) 229–255, https://doi.org/10.1142/S1363246905002365.
[63] N.R. Barton, V. Choubey, The Shear Strength of Rock Joints in Theory and Practice, Rock Mech. 10 (1977) 1–54, https://doi.org/10.1007/BF01261801.
[64] M. Lavella, Contact Properties and Wear Behaviour of Nickel Based Superalloy Rene 80, Metals (Basel) 6 (2016), https://doi.org/10.3390/met6070159.
[65] S. Allaoui, A. Rekik, A. Gasser, E. Blond, K. Andreev, Digital Image Correlation measurements of mortarless joint closure in refractory masonries, Constr. Build. Mater. 162 (2018) 334–344, https://doi.org/10.1016/j.conbuildmat.2017.12.055.
[66] R. Brincker, C.E. Ventura, Introduction to Operational Modal Analysis, John Wiley & Sons (2015), https://doi.org/10.1002/9781118535141.
[67] D.J. Ewins. Modal Testing: Theory, Practice and Application, 2000. ISBN: 978-0-863-80218-8, https://www.wiley.com/en-be/Modal+Testing:+Theory,+Practice+and+Application,+2nd+Edition-p-9780863802188.
[68] J.P. Noël, G. Kerschen, Nonlinear system identification in structural dynamics: 10 more years of progress, Mech. Syst. Signal Process. 83 (2017) 2–35, https://doi.org/10.1016/j.ymssp.2016.07.020.
[69] R. Brincker, S. Krenk, P.H. Kirkegaard, A. Rytter, Identification of Dynamical Properties from Correlation Function Estimates, Danish Soc. Struct. Sci. Eng. 63 (1992) 1–38. https://vbn.aau.dk/en/publications/identification-of-dynamical-properties-from-correlation-function-.
[70] R. Brincker, C.E. Ventura, P. Andersen, Damping Estimation by Frequency Domain Decomposition, in: Proc. IMAC 19, 2001.
[71] F. Magalhães, Á. Cunha, E. Caetano, R. Brincker, Damping estimation using free decays and ambient vibration tests, Mech. Syst. Signal Process. 24 (2010) 1274–1290, https://doi.org/10.1016/j.ymssp.2009.02.011.
[72] R.J. Allemang, The modal assurance criterion - Twenty years of use and abuse, Sound Vib. 37 (2003) 14–21. http://www.sandv.com/downloads/0308alle.pdf.
[73] H. Schmidt, Resolution bias errors in spectral density, frequency response and coherence function measurements, I: General theory, J. Sound Vib. 101 (1985) 347–362, https://doi.org/10.1016/S0022-460X(85)80135-8.
[74] C. Rainieri, G. Fabbrocino, E. Cosenza, Some remarks on experimental estimation of damping for seismic design of civil constructions, Shock Vib. 17 (2010) 383–395, https://doi.org/10.3233/SAV-2010-0534.
[75] F. Lorenzoni, N. De Conto, F. da Porto, C. Modena, Ambient and free-vibration tests to improve the quantification and estimation of modal parameters in existing bridges, J. Civ. Struct. Heal. Monit. 9 (2019) 617–637, https://doi.org/10.1007/s13349-019-00357-4.
[76] L. Pastewka, N. Prodanov, B. Lorenz, M.H. Müser, M.O. Robbins, B.N.J. Persson, Finite-size scaling in the interfacial stiffness of rough elastic contacts, Phys. Rev. E 87 (2013) 1–10, https://doi.org/10.1103/PhysRevE.87.062809.
[77] B.N.J. Persson, Relation between interfacial separation and load: A general theory of contact mechanics, Phys. Rev. Lett. 99 (2007) 1–4, https://doi.org/10.1103/PhysRevLett.99.125502.
[78] C.H. Scholz, S.H. Hickman, Hysteresis in the Closure of a Nominally Flat Crack, J. Geophys. Res. Solid Earth. 88 (1983) 6501–6504, https://doi.org/10.1029/JB088iB08p06501.
[79] DIANA FEA, User's Manual - Release 10.5, DIANA FEA BV., 2021. https://dianafea.com/manuals/d101/Diana.html.
[80] H. Gercek, Poisson's ratio values for rocks, Int. J. Rock Mech. Min. Sci. 44 (2007) 1–13, https://doi.org/10.1016/j.ijrmms.2006.04.011.